Enhanced Filterbanks for THz On-Chip Spectrometers

Louis Marting

Delft University of Technology

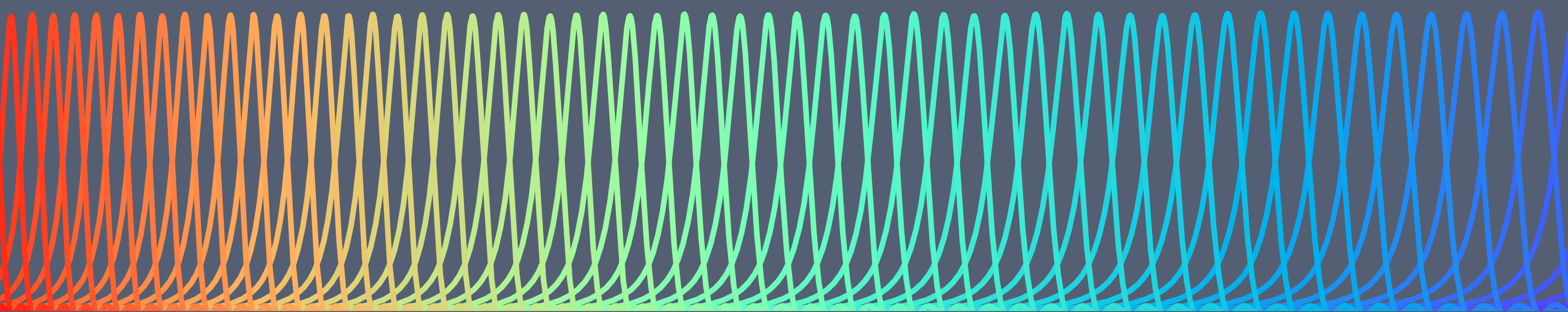

TU Delft

Enhanced Filterbanks for THz On-Chip Spectrometers

by

Louis Marting

to obtain the degree of Master of Science
at the Delft University of Technology,
to be defended publicly on Friday September 9, 2022 at 12:30 PM.

Student number:	4445600	
Project duration:	August 30, 2021 – September 9, 2022	
Thesis committee:	Prof. dr. ir. J. J. A. Baselmans,	TU Delft, supervisor
	Dr. M. Spirito,	TU Delft
	Dr. A. Pascual Laguna,	TU Delft, daily supervisor

Cover:	Simulation of an on-chip filterbank
Style:	TU Delft Report Style, with modifications by Daan Zwaneveld and Louis Marting

An electronic version of this thesis is available at `http://repository.tudelft.nl/`.

Abstract

Terahertz astronomy has been exceptionally unexplored until the last decades due to a technological gap, but exactly at these wavelengths the most distant galaxies appear very bright. Efficient instruments that are capable of spectrometry are essential in understanding the physics of these distant objects. Within the framework of this thesis, an efficient, moderate spectral resolution, on-chip filterbank spectrometer is presented. Several band-pass filter units were investigated and compared, being the directional band-pass filter the most robust and performing. A circuit model is constructed for each of these units and arrayed into a filterbank configuration resorting to microwave techniques. The performance of the filterbank with the circuit model, both with and without realistic losses and tolerances is modeled. A microstrip directional band-pass filter unit has been designed and arrayed into a filterbank chip design. A test filterbank chip based on this design has been fabricated. Due to fabrication issues the detector yield was too poor to allow in-depth and statistically significant measurements. Despite this, the filterbank design is expected to outperform state-of-the-art superconducting filterbanks in terms of coupling efficiency.

Contents

Abstract **i**

1 Introduction **1**
1.1 THz Astronomy . . . 2
1.1.1 Key Science . . . 4
1.2 Instrument Requirements . . . 5
1.2.1 Spectrometer Requirements . . . 5
1.2.2 MKID Detectors . . . 7
1.3 Problem Statement . . . 9
1.4 Thesis Outline . . . 9

2 Band-Pass Filter Concepts for On-chip Filterbank Spectrometry **11**
2.1 Band-Pass Filter Concepts . . . 12
2.1.1 General Introduction to Band-Pass Filters . . . 12
2.1.2 Manifold Filter . . . 13
2.1.3 Reflector Filter . . . 14
2.1.4 Directional Filter . . . 15
2.2 Filterbank Model . . . 16
2.2.1 Comparison of Filter Concepts . . . 18
2.3 Conclusion . . . 20

3 Modelling Tolerances and Losses of a Filterbank Spectrometer **21**
3.1 Variances in the Filterbank Model . . . 21
3.1.1 Method . . . 22
3.1.2 Results . . . 24
3.2 Losses in the Filterbank Model . . . 27
3.3 Conclusion . . . 28

4 Chip Design **29**
4.1 Filter Design . . . 29
4.1.1 Vertically stacked coupling structure . . . 31
4.1.2 Filter Simulation Compared to Model . . . 34
4.2 MKID Design . . . 34
4.3 Test Chip . . . 37
4.3.1 Design . . . 37
4.3.2 Fabrication . . . 38
4.3.3 Over-Etching . . . 38

4.3.4 Step Coverage 40

5 Preliminary Experimental Results of a Test Chip 41

5.1 Method 41

5.2 Results 42

5.3 Discussion 44

5.3.1 Silicon Carbide Over-Etch 44

5.3.2 Optical and Electron-Beam Patterning Misalignment 45

6 Conclusions and Outlook 47

6.1 Conclusions 47

6.2 Outlook 48

References 49

A Size Comparison of Spectrometers 52

B Calculations to find the Coupling Capacitor Strength and Resonator Length 54

B.1 Coupling Strength 54

B.1.1 Ideal Capacitor 55

B.1.2 Simulated Coupling Structure 56

B.2 Resonator Length 56

C Filterbank Model Results 57

D Filterbank Model Results with Variances 59

1
Introduction

Astronomers have long been interested in the star-forming galaxies at the cosmic dawn of the early Universe. The cosmic dawn is when the first stars formed, about 300 million years after the Big Bang. The study of these galaxies promises to explain the past, present, and future of our galaxy and the Universe. In particular, the spectroscopy of these galaxies allows us to resolve their distance, detect the presence of certain chemicals and probe their physics. The radiation from these far-away sources is brightest in the THz band, which we will define here from 30 GHz to 1 THz. This frequency range is neighboured by the microwave band at lower frequencies and far infrared (FIR) radiation at higher frequencies.

Historically, this band has proven to be very difficult to observe for a number of reasons. Coherent spectroscopy has a very high spectral resolution, but suffers from narrow relative bandwidth and can only observe tiny cosmological volumes [1]. Cameras based upon direct detectors, such as SCUBA-II [2] have captured broadband images of these early galaxies, but broadband direct detector spectrometers, based upon dispersive optics and large format detector arrays, are too bulky and complex to realistically operate for higher frequency resolutions and large bandwidths in the THz band. In essence, further development of broadband spectroscopy instruments in the THz band is needed to capture the redshift information of these far-away sources and explain the science of the early Universe.

An integrated field unit (IFU) instrument is the solution to this problem, it can capture a wide field-of-view with a sufficient spectral resolution. An IFU is a multi-pixel spectrometer, an illustration of the concept for an on-chip filterbank configuration is seen in Figure 1.1. Single pixel devices in the THz band demonstrate good promise towards the creation of these IFUs, the superconducting on-chip filterbank spectrometer being the most promising. Advances in nanotechnology and the maturation of detector technology have yielded a number of on-chip spectrometers, such as Super-SPEC [3], W-SPEC [4], µ-SPEC [5], DESHIMA [6] and CAMELS [7]. DESHIMA is the only on-chip spectrometer that was successfully fielded on a telescope [8]. These instruments have proven that the on-chip spectrometer concept can ideally be used for broadband spectroscopy of the THz band. This early success has driven the quest for the development of an IFU in the THz band.

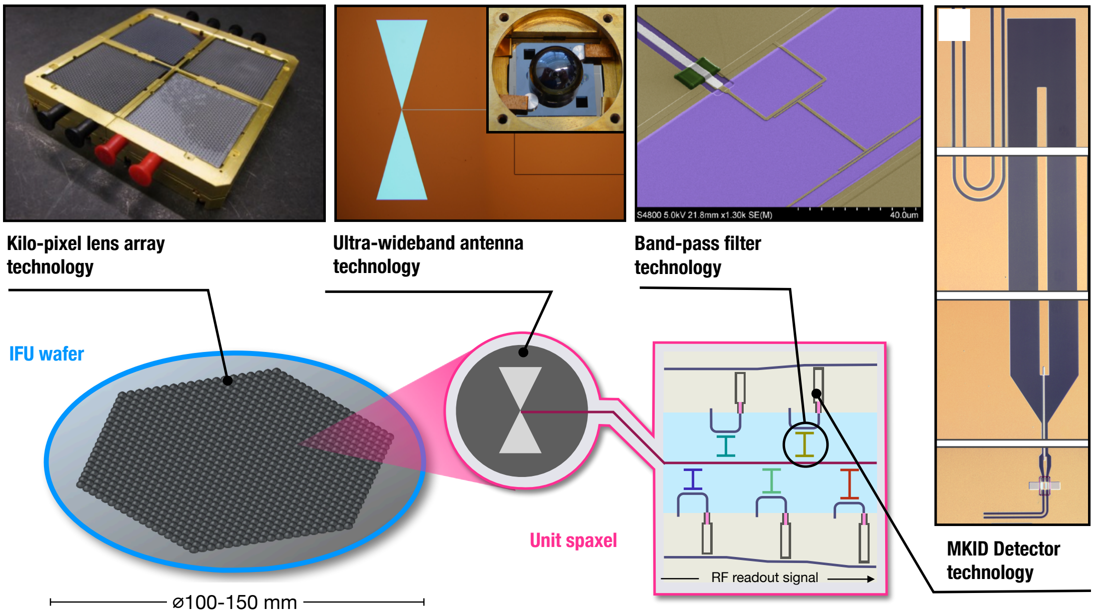

Figure 1.1: A concept of a superconducting IFU using an on-chip spectrometer. Illustration courtesy of A. Endo.

An IFU is efficient for a number of astronomical applications: 1) Observations of dusty star-forming galaxies; 2) A survey of terahertz line emitting galaxies; 3) Large scale structure of cold interstellar matter; 4) Sunyaev-Zeldovich effect measurements for cluster physics. Only such highly integrated devices can explore these science cases effectively. A single on-chip instrument will support a multiplexity that is unmatched. These devices will have hundreds of spatial pixels, (multi-)octave instantaneous bandwidths and a spectral resolution up to about 1000. With a realistic detector count of $\sim$ 10,000, a large degree of flexibility is provided for these IFUs.

1.1 THz Astronomy

The expansion of the Universe is ever continuing. Distant galaxies are moving further away from us since its creation. It so happens to be that light from these distant sources still is able to reach us, as has been established by the Special Theory of Relativity proposed by Einstein [9]. This light has travelled for billions of years, allowing us a peek into the history of our Universe. The expansion of the Universe over time effectively stretches the light, which is known as redshift. The definition of redshift is given by

$$z = \frac{\lambda_o}{\lambda_e} - 1. \tag{1.1}$$

Here, λ_o and λ_e are the observed and emitted wavelengths, respectively. Redshift is the name given to the wavelength increase of the arriving light due to the expanding space which the light travels through between the source and us. This phenomenon has been used for many astronomical applications, one of which is the observation of galaxies in the early Universe.

Light from star-forming galaxies in the early Universe is difficult to detect, as it is obstructed by dust. An alternative to the observation of the visible light is to observe the emission from the cool interstellar gas. This gas mainly consists of hydrogen, with traces of carbon, oxygen, and nitrogen in various states, as well as dust particles. This gas has a temperature of around 40° K and emits black-body radiation in the FIR. Besides this, these molecules absorb and re-emit the energy from the surrounding stars, appearing as narrow line emissions. The most luminous of these is the ionized carbon [C_{II}] emission at 1.9 THz, accounting for up to 1% of the total luminosity of the galaxy.

An example of an emission spectrum of a galaxy for different redshifts can be seen in Figure 1.2. Using spectroscopy to detect these galaxies has clear advantages. The bandwidth observed is cut up in many slices, and the light of these narrow line emissions will light up a few detectors strongly. The spectrometer will be able to detect these sources much faster than a broadband detector, since the line emissions are not flooded by the noise outside the narrow band of the line emission.

Furthermore, the line emission detection of these high-z galaxies is used to accurately determine its redshift. Since the frequency of this line emission is known in a rest frame (namely 1.9 THz for [C_{II}]), we must only observe the peak frequency of this line emission and accurately calculate its redshift using Equation 1.1.

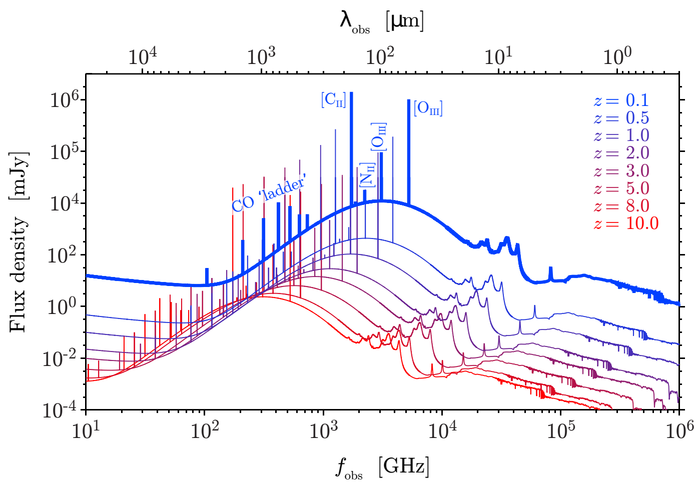

Figure 1.2: Typical emission spectrum of a FIR galaxy, image adapted from [10]. The most prominent emission line features are marked. Note that between 100 GHz and 1 THz the Flux density is similarly intense regardless of redshift.

This forms the basis of THz astronomy and allows us to peer into the early Universe between redshifts of z= 1 to 10. Not only can we observe redshifts of these galaxies accurately, but their cool gas is also where new stars are born. Therefore, the detection of these line emissions and their relative strength with regard to the broadband emission can probe star formation in these early galaxies. With this framework, astronomers have developed several key science cases that only THz astronomy can attempt to answer.

1.1.1 Key Science

While the observation of single sources in the THz band have been performed accurately, never have there been unbiased large scale surveys of high-z galaxies that are brightest in the THz band. Surveys of high-z galaxies using X-ray emissions have been biased to high-mass systems, making it hard to generalize the conditions in the early Universe from these results. Successes such as the Sloan Digital Sky Survey [11] in the visible band have not been recreated in our frequency band of interest so far. This is due to the simple fact that highly efficient imaging spectrometers do not exist for the THz band. These highly integrated imaging spectrometers, or IFUs, are needed to measure the large volumes of sky for an unbiased measurement in a reasonable time. If a sub-mm/THz IFU can be realized, it will open the door to the following key science cases:

1. Observations of single dusty star-forming galaxies at high z.
2. Survey of line-emitting galaxies that have a faint continuum spectrum.
3. Large scale structure of interstellar matter by measuring line emission fluctuations without resolving individual galaxies.
4. Measurement of the Sunyaev-Zeldovich effect to understand cluster physics.

Observations of individual dusty star-forming galaxies

The observation of individual dusty star-forming galaxies tries to precisely measure the redshift of far away galaxies, and the intensity of the line emissions that they radiate. Being able to quickly observe many individual galaxies with high detail will allow us to say more about the star formation rate at these high red-shifts. Allowing us to better explain the structure of the Universe that we see now.

Survey of line-emitting galaxies

Up until now, large cosmic volume surveys of the sub-mm/THz region only captured wideband spectral information. This is useful for observing the continuum spectrum, but is unsuited for line emission detection. This has potentially caused these observations to miss galaxies that have a faint continuum spectrum, but a bright line-emission spectrum. This survey aims to correct that by looking at a few redshift slices with a moderately high resolution across a large cosmic volume. This should give a better overview of the abundance of dusty galaxies across our early Universe.

Large scale structure of interstellar matter

Besides detection and classification of individual galaxies, it is also useful to observe the overall variation of line emission intensity across the night sky. A measurement of the large scale structure could uncover patterns between this observation and other large scale structures previously observed.

Measurement of the Sunyaev-Zeldovich effect
Lastly, the measurement of the Sunyaev-Zeldovich (SZ) effect can tell us more about the physics that are present in clusters. The SZ effect changes the apparent brightness of the black-body radiation of the cosmic microwave background. This in turn can be combined with data from X-ray measurements to tell us more about the dynamics at play in these largest structures of the Universe.

1.2 Instrument Requirements

In order to realize the IFUs to do science, the size of the spectrometer, to be located behind each pixel, needs to be small. Compared to established single pixel spectrometer designs, the on-chip spectrometer has several orders of magnitude smaller footprint (see Appendix A). It is therefore the ideal spectrometer concept to be used in the IFU. Finally, the detector technology used, called microwave kinetic inductance detectors (MKIDs), has shown high sensitivity and multiplexing capabilities needed for the realization of these IFUs. First, the requirements of the spectrometers used in the IFU are specified. Second, a brief description of the MKID technology is given.

1.2.1 Spectrometer Requirements

In Figure 1.3 an illustration of an on-chip filterbank spectrometer can be seen. The THz signal is coupled to the chip using a lens antenna. Here, the filter is split using a number of band-pass filters with a detector (MKID) behind them.

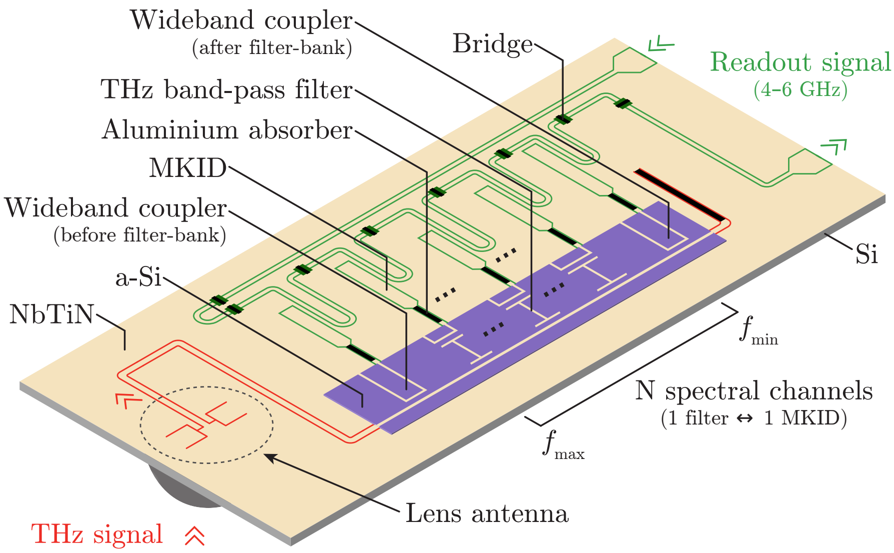

Figure 1.3: Illustration of an on-chip filterbank spectrometer. Image courtesy of A. Pascual Laguna.

Each of the four science cases have different requirements with regard to the spectral resolution, R, the number of pixels, N_{pixels}, and the bandwidth, B, that needs to be covered. Table 1.1 summarizes the design space. These three parameters, combined with the realistic total detector count of $\sim$ 10,000, form the design space for an instrument.

For the purpose of designing an on-chip spectrometer, the bandwidth and spectral resolution are most important. The resolution must be high enough to disambiguate the spectral features that we would like to detect, such as the line emissions of redshifted emission lines. The spectral resolution is defined as

$$R = \frac{f_0}{\Delta f}, \tag{1.2}$$

where f_0 is the central frequency and Δf is the full-width half-maximum bandwidth around f_0. The instrument must be able to operate over a wide bandwidth, since the redshifted line emission can appear at many frequencies. We define bandwidth as the difference between the highest (f_{max}) and lowest (f_{min}) observing frequencies:

$$B = f_{\mathrm{max}} - f_{\mathrm{min}}. \tag{1.3}$$

An octave instantaneous bandwidth is currently feasible with the antenna and filter-bank designs to-date.

Together, these two parameters form the basis for the number of filters (and detectors) that need to be designed. Assuming a sampling of the bandwidth B with filter response cross-overs at 50% of their maxima, the filter central frequencies are given by

$$f_i = f_{\mathrm{max}}(1 + R^{-1})^{-i+1}, \tag{1.4}$$

where $f_{\mathrm{max}} = f_{\mathrm{min}}(1 + R^{-1})^{N_{\mathrm{filters}}-1}$ and the number of filters is given by

$$N_{\mathrm{filters}} = \left\lceil \frac{\log(f_{\mathrm{max}}/f_{\mathrm{min}})}{\log(1 + R^{-1})} \right\rceil. \tag{1.5}$$

On-chip spectrometers bring with them significant flexibility in terms of the number of pixels, the spectral resolution and the bandwidth. Normally, this would require several devices that are custom-built and hard to interchange. For the on-chip spectrometer IFU, the only thing that needs to be swapped is the chip. These chips are characterized very well and designing them will be relatively straightforward.

Lastly, the number of pixels (N_{pixels}) should be as high as possible. There is a spectrometer behind each pixel, therefore, integrating many pixels with spectrometers in a single device will save a tremendous amount of measurement time. Table 1.2 shows how the spectral resolution, instantaneous bandwidth, and number of pixels could be traded off for each science case.

Parameter	Description
N_{pixels}	Number of pixels
R	Spectral resolution
B	Observed bandwidth

Table 1.1: Design space for the IFU instrument.

Key Science	R	B	N_{pixels}	N_{filters}
Dusty star-forming galaxies	1000	$1:4$	7	693
Line-emitting galaxies survey	500	$10\% \times 3$	91×2	119
Line intensity mapping	100	$1:1.9$	169×2	62
Sunyaev-Zeldovich effect measurement	10	$1:4$	$61 + 217$	7

Table 1.2: Combinations of parameters for each key science case. Note the trade-off between N_{pixels} and N_{filters} For the middle two cases, N_{pixels} is given for two polarizations. The parameter combinations are given by A. Endo in private communications and form the basis for a number of proposed IFU designs.

1.2.2 MKID Detectors

Microwave kinetic inductance detectors, or MKIDs, are superconducting pair breaking detectors. They are especially interesting for IFUs for two reasons. First, they allow for very large arrays, by using microwave division readout, allowing up to 10,000 detectors per single readout channel. Second, they reach a sensitivity limited only by the photon flux falling on the detector. A brief description of how they work is given here, and their aspects relevant to this thesis are explained. For an in-depth description, one of the following readings is recommended: [12], [13].

Figure 1.4 shows the basic concept of an MKID detector. MKIDs work on the basis of a superconducting resonator at microwave frequencies. In a superconducting state, the paired electrons, called Cooper pairs, conduct the signal without losses [14]. The resonator has a very high Q-factor, due to the low losses associated with the superconducting state. The Cooper pairs, subject to the oscillating field, have inertia due to the mass of the electrons. This inertia creates a "kinetic inductance", an inductance due to the mass of the electrons subject to the oscillating field. The kinetic inductance is referenced with the parameter L_{k}.

To detect a THz signal, Cooper pairs are broken in the resonator. The remaining Cooper pairs need a higher velocity to keep the current through the superconductor equal. This results in a larger inertia and a larger kinetic inductance, which lowers the resonance frequency slightly. Due to the high Q-factor of the resonance, the tiny change in resonance can be detected.

In a typical setup for a spectrometer, the MKID detector is placed behind a filter. Here, the THz signal emerging from this filter is coupled to the hybrid CPW section of the MKID resonator. Where the aluminium center line allows for Cooper pair breaking at THz frequencies, but is superconducting at the microwave frequencies at which the MKID is resonating. A readout tone is placed at the unloaded resonance frequency, and any changes in the resonance frequency are recorded by a change in amplitude and phase.

The sensitivity of detection instruments for space observation (such as MKIDs) is given by the noise equivalent power (NEP). It is described briefly, without going into much detail. The NEP is defined as the signal power that can be detected with an SNR of 1 for 0.5s of integration time. The detector can operate between two input signal extremes, which change the dominant terms in the NEP. A detector can be signal limited, this

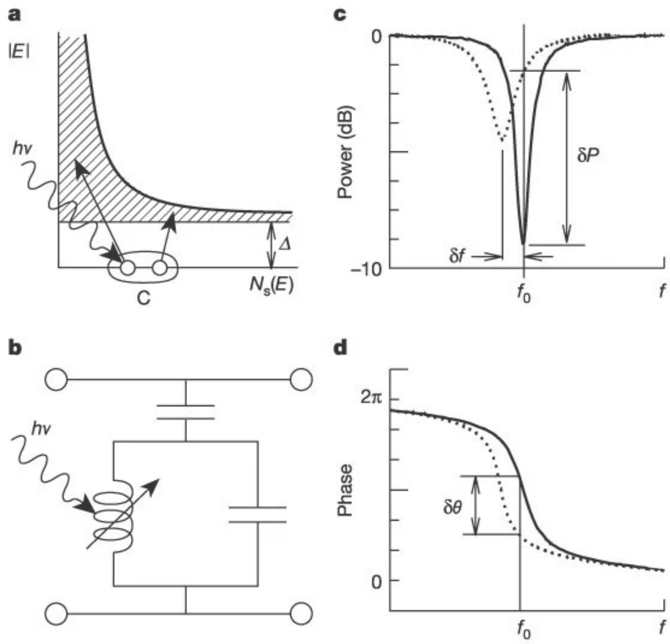

Figure 1.4: The basic concept of an MKID detector, as first proposed by [15]. **(a)** Shows incoming radiation being absorbed, breaking Cooper pairs. **(b)** Shows the resonance dip that occurs on the readout line, due to the loading of the MKID resonator on its resonance. When radiation is absorbed, the amplitude of the signal shifts at the readout tone (f_0). **(c)** Shows the circuit model of an MKID, where absorption of radiation causes a change in L_s and R_s of the resonator. **(d)** Shows how the shift in resonance frequency due to absorption causes a shift in the phase of the resonator at the readout tone (f_0).

means that the power contribution of the signal of interest is significant to the total power on the detector. This is mainly applicable for instruments in space. The detector can also be background limited. In this case, the total power on the detector is almost exclusively determined by the background, i.e. radiation from all sources but the signal of interest. For ground based astronomy, detectors are always background limited, since the atmosphere emissions loads detectors significantly.

Given that the instrument and its detectors are installed on a ground based telescope, the background limited (BLIP) NEP for an MKID can be given as

$$NEP_{\mathrm{BLIP}} = \sqrt{2P_{\mathrm{MKID}}hf_0 + 2\frac{P_{\mathrm{MKID}}^2}{\Delta f_0} + 4\Delta_{\mathrm{Al}}\frac{P_{\mathrm{MKID}}}{\eta_{\mathrm{pb}}}}, \tag{1.6}$$

where P_{MKID} is the power incident on the detector, h is the plank constant, Δ_{Al} is the superconducting band-gap of aluminium, and η_{pb} is the Cooper pair breaking efficiency. This formula is a limit of the formal physical definition of the NEP for such a detector based on the operation of the instrument in an on-chip filterbank configuration [8]. The NEP for an MKID has three terms. The Poisson term, the bunching term, and the generation-recombination (GR) noise term, respectively. The Poisson term and bunching term represent noise due to the properties of the incoming light. The GR noise term comes from the random breaking apart and recombination of Cooper pairs due to thermal fluctuations in the detector.

The NEP of MKID detectors is very good for the THz band, and the high muliplexity of MKIDs make them suited for making large arrays. The MKID is the ideal detector for making single pixel on-chip spectrometers and, in the future, IFUs.

1.3 Problem Statement

Current on-chip filterbank spectrometers suffer a poor filter efficiency due to the design of the filters. Typically, these filter-banks use shunted, capacitively-coupled, half-wave resonators as band-pass filters. An ideally matched shunted filter will only capture 50% of the power in a theoretical ideal situation. However, the losses and fabrication tolerances further reduce the coupling to about 27% [16]. The poor efficiency makes that current instruments are losing photons from our astronomical object of interest, and it requires more sensitive detectors and longer measurement times.

A better on-chip filter design has to be realized which can reach efficiencies beyond 80%. New filter concepts need to be explored that can overcome this fundamental problem. This thesis aims to find alternative filter concepts that can improve the performance of the on-chip filterbank spectrometer.

1.4 Thesis Outline

This thesis will propose a number of promising filter concepts that are able to improve upon the currently used filters. A circuit model is made to accurately model their behaviour. Using this model, the filter concepts are tested against realistic fabrication tolerances. One filter concept is chosen and fabricated into a test chip. This test chip is measured and characterized, and the measurements are compared to the model.

In Chapter 2 two new filter concepts are introduced. Each filter concept is evaluated in isolation and when placed in a filterbank. A circuit model is constructed using microwave techniques to help characterize the performance of each concept. The circuit model is a time efficient way of synthesizing new filterbank designs.

In Chapter 3 the tolerances and losses that are present in any fabricated filterbank are modelled. Variances are added to the resonance frequency and spectral resolution of the filters and put into the circuit model to evaluate these effects. Furthermore, losses are added to the model to observe their effects. From this analysis, one filter concept, the directional filter, is chosen to be fabricated in a test chip.

In Chapter 4 the design of the directional filter is detailed. A vertical coupling structure is used to minimize the coupling variances and SiC is used as a low-loss dielectric between the layers. This design is implemented in a full test chip spanning 200 GHz to

400 GHz, with a spectral resolution of 100. The test chip is fabricated.

In Chapter 5 the fabricated chip is measured and, due to a poor yield, a discussion is held on the point of failure. Recommendations are given to improve the design.

In Chapter 6 the conclusions of this thesis are given, and an outlook is given for future research.

2

Band-Pass Filter Concepts for On-chip Filterbank Spectrometry

An on-chip spectrometer must split a broadband signal into many small bands. Often, the spectral resolution and bandwidth requirements lead to a spectrometer with many filters, as dictated by Equation 1.5. The most practical layout to split the signal in so many bands is shown in Figure 2.1. Incoming radiation is captured by an antenna and then transferred to a transmission line. Blocks of filtering elements split the in-band signal from the out-band signal, sending the in-band signal to a detector and the out-band signal to the next block. Each block is tuned to a different frequency. The remaining signal is absorbed in a terminating absorber.

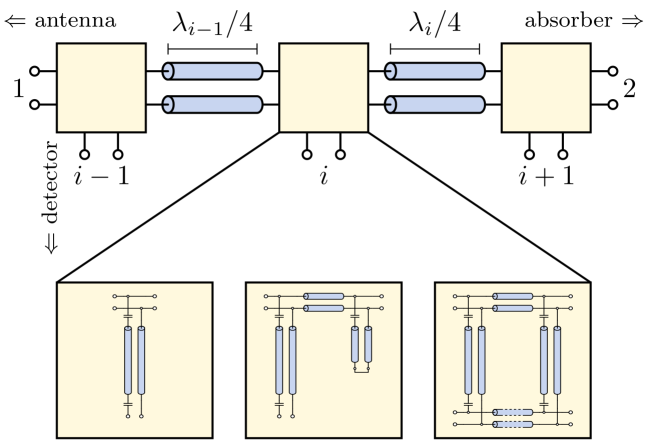

Figure 2.1: A black box schematic of a filterbank concept. Several filter concepts can be used to filter the signal to many detectors. Each filter is separated from its neighbours by a quarter-wave section to prevent reflections and spurious resonances.

A strong requirement of an on-chip spectrometer is to minimize the disturbance of the wideband signal, since any small disturbance or source of losses on the wideband signal will accumulate. To prevent this, the THz-line is usually kept free of filtering elements (e.g. stubs, resonators, impedance changes). This allows the signal line carrying the wideband signal to be one continuous transmission line, which we will call the THz-line.

Conventionally, on-chip filterbank spectrometers have been constructed using half-wave resonators for filters [3], [16]. These filters are capacitively coupled to the THz-line. The devices are connected in shunt and act as a band-pass filter, to couple a specific frequency range to the detector. However, we are not limited to using simple capacitively-coupled half-wave resonators. Figure 2.1 shows how we can replace the standard half-wave resonator with alternatives, which we will come to shortly.

2.1 Band-Pass Filter Concepts

First, the basic concept of a half-wave resonator is explained, since this forms the basis of all our filter concepts. Then, each filter concept is introduced, detailing their advantages and disadvantages. Their frequency response is shown using a circuit model constructed using microwave techniques. In Section 2.2, a circuit model is constructed of a full filterbank for each filter concept, simulating the effect that neighbouring filters have on each other.

2.1.1 General Introduction to Band-Pass Filters

Figure 2.2 shows a schematic of the capacitively coupled half-wave resonator. The filter consists of three elements. Two couplers, one at the THz-line and one at the detector, and a piece of transmission-line with a length of about a half-wavelength on resonance $\lambda_0/2$. The loaded quality factor (Q-factor) is a measure of the energy leakage per cycle and is equal to the spectral resolution, R, of the filter, given by

$$Q_{\mathrm{L}} = 2\pi f_0 \frac{E_{\mathrm{stored}}}{P_{\mathrm{lost}}} = \frac{f_0}{\Delta f_0} = R, \tag{2.1}$$

where E_{stored} is the average energy stored in the resonator per cycle and P_{lost} is the power lost per cycle. The in-band transmission of a resonator is given by Δf_0 and is defined as the full-width half-maximum (FWHM) of the resonance peak.

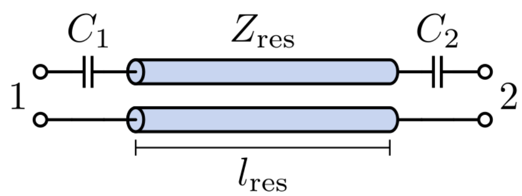

Figure 2.2: circuit model of a coupled half-wave resonator. The capacitors couple energy to and from the resonating element.

The loaded Q-factor of the filter can be calculated using the quality factors of the comprising elements. The resonator itself has dielectric losses. This is an internal energy loss mechanisms that limits the performance of the filters, and it can be captured in the internal quality factor, Q_i. The couplers C_1 and C_2 are capacitively exchanging energy between the resonator and both the THz-line and the detector. Per cycle, they exchange a certain amount of energy, which can be modelled with the coupling quality factor. Since there are two couplers, we will have a quality factor for each, Q_{C_1} and Q_{C_2}. Using the Q-factors of each element, the loaded Q-factor can be expressed as

$$Q_\mathrm{L}^{-1} = Q_\mathrm{i}^{-1} + Q_{C_1}^{-1} + Q_{C_2}^{-1}. \tag{2.2}$$

For maximum on-resonance transmission, the coupling quality factors need to be equal [17]. From the equation above, the value of the coupling quality factors is derived as

$$Q_{C_1} = Q_{C_2} = \frac{2Q_\mathrm{i}Q_\mathrm{L}}{Q_\mathrm{i} - Q_\mathrm{L}}. \tag{2.3}$$

Using this formula and given a certain Q_i, the coupling capacitors can be designed to achieve a desired Q_L (which is equal to the spectral resolution of the filter).

Finally, the length of the resonator (l_res) can be determined, given the resonance frequency f_0. The length of the resonator under loading will be slightly less than $\lambda_0/2$. The coupling capacitors combined with the load of the connecting transmission lines add a bit of phase to the resonant circuit [18]. Therefore, for the same resonance frequency, the loaded resonator length is slightly shorter than the unloaded length of $\lambda_0/2$. The length of the resonator using the known loading of the couplers is calculated by setting the imaginary part of the input impedance to be zero. In Appendix B the calculations for the coupling capacitor strength and resonator length are given in detail.

2.1.2 Manifold Filter

The manifold filter concept is constructed by connecting a half-wave resonator in shunt to the THz-line. The transmission line model of the filter concept can be seen in Figure 2.3a. The transmission line model shows two pieces of the THz-line connecting at the top node where the half-wave resonator connects. These pieces left and right of the node are the incoming and outgoing transmission lines of the THz-line, respectively. These load the half-wave resonator in parallel, resulting in the loading at the THz-line side being equal to $Z_L^\mathrm{THz} = Z_0^\mathrm{THz}/2$.

The S-parameters of the transmission line model are shown in Figure 2.3b. The peak transmission of this filter on resonance is 50%. Without losses, 50% transmission is the fundamental upper limit of this filter concept. Of the remaining power, 25% is reflected towards the antenna and the final 25% is transmitted in the absorber direction. This limit can be attributed due to the loading conditions on-resonance. On resonance, the resonator can be seen as an energy storing mechanism that leaks away continuously through its couplings and its internal quality factor. Since the coupling Q-factors are equal, an equal amount of energy leaks from the resonator on both sides. On the detector side, this power is absorbed in the detector. On the THz-line side, the resonator sees two

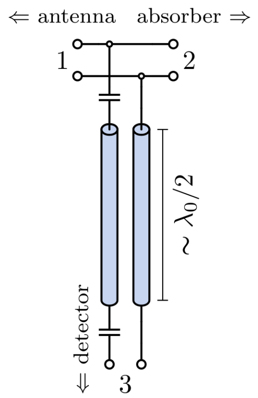

(a) Circuit model of a manifold filter concept.

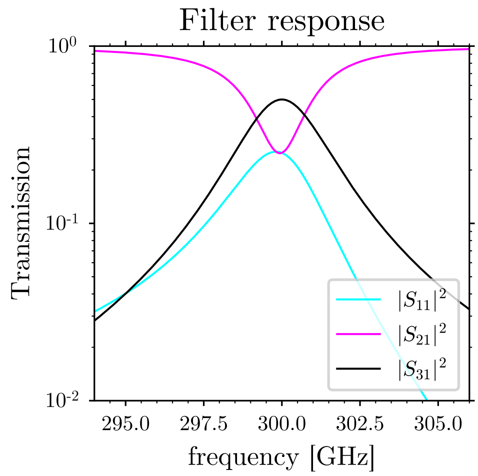

(b) Frequency response of a manifold filter concept around its resonance frequency.

Figure 2.3: The manifold filter concept

transmission-lines connected in parallel. The remaining 50% power, is divided equally over these two transmission-lines.

The simplicity of the manifold filter make it the easiest filter to implement. The transmission line model can easily be implemented using microwave techniques, which gives this concept a well bounded design space and useful equations to interpret measurements, which makes it a safe filter concept for designing a filterbank. To improve the efficiency above 50%, a filter concept that is better matched to the THz-line needs to be used. Two alternatives to the capacitively coupled half-wave resonator are proposed. These are the reflector filter in Section 2.1.3 and the directional filter in Section 2.1.4.

2.1.3 Reflector Filter

The reflector filter is based on an idea proposed by [4], [19]. A schematic of the reflector filter can be seen in Figure 2.4a. Starting from a manifold filter concept, an extra, short-circuited, quarter-wave resonator is placed at $\lambda/4$. The short-circuited resonator is capacitively coupled to the THz-line and on-resonance the input impedance of this section will drop to zero, shorting the THz-line. Since this impedance condition is placed at $\lambda/4$ from the half-wave resonator, it will be transformed to an open circuit condition at the reference plane of the half-wavelength band-pass filter. In other words, on-resonance, the band-pass filter does not observe the trailing THz-line, and it appears as if the filter is connected in series with the incoming in-band signal. The in-band signal is blocked from reaching any following filters.

In Figure 2.4b the S-parameters of the reflector filter concept can be seen. This filter concept has the best sidelobe tapering of all designs, meaning that less power is absorbed outside the designed band. The efficiency of this filter reaches 100% on resonance, doubling the maximum efficiency compared to the manifold filter. The use

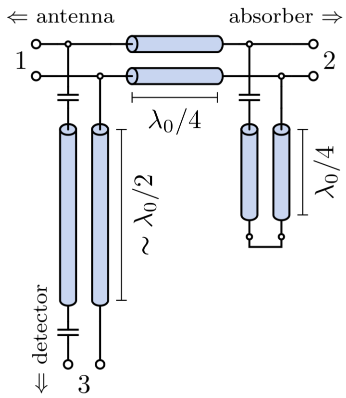

(a) Circuit model of a reflector filter concept.

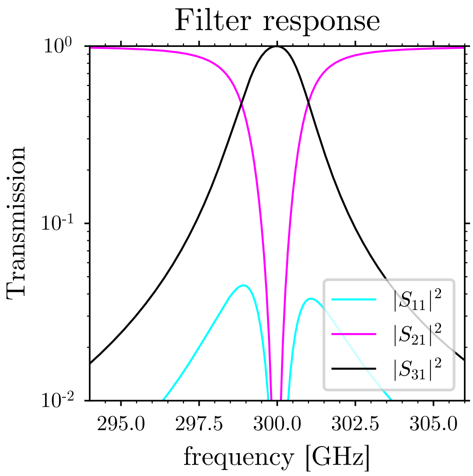

(b) Frequency response of a reflector filter concept around its resonance frequency.

Figure 2.4: The reflector filter concept

of shorted resonators makes this design vulnerable to small fabrication variances. The resonance of the filter must be tuned exactly to the resonance of the short. If there is a frequency offset, potentially large reflections can occur on the THz-line, since the reflector will reflect power which is not efficiently captured by the filter. Adding the shorted quarter-wave resonator to the circuit is relatively simple to implement. Only an extra resonator is needed. Furthermore, the addition of this resonator increases the spacing between detectors to $\lambda/2$ instead of $\lambda/4$.

2.1.4 Directional Filter

The directional filter concept uses a far more integrated design than the previous two concepts. The directional filter name and concept originates from several papers from the 1950s [20]–[23]. These structures were used in microwave systems to multiplex channels. This allowed for directional specific filtering of the signal. A circuit model of the concept can be seen in Figure 2.5a The structure is made up of two resonators, which are capacitively connected to the THz-line and are separated in the THz-line by $\lambda/4$. On the detector side, the coupling is spaced by $3\lambda/4$. This structure is vertically symmetric. The response of this structure can be rigorously solved using the impedance matrix or by using the even/odd-mode analysis [18]. Here, the response is found by using the impedance matrix.

In Figure 2.5b, the S-parameters of the directional filter concept can be seen. This concept is able to capture all energy on-resonance, reaching 100% efficiency. The structure has two output ports (ports 3 and 4). The isolated output port is always diagonal to the driven port. If port 1 is driven, port 4 will be isolated. If the design is not perfectly matched, some power will leave port 4. Therefore, the power that is output from both ports needs to be captured in the detector. The filter response plotted is the sum of

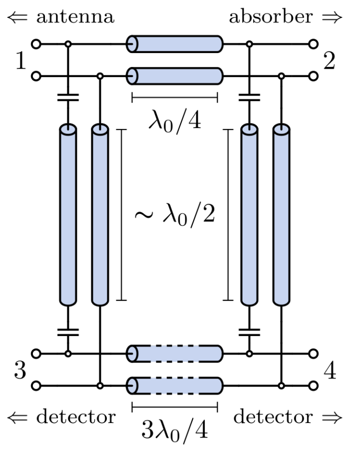

(a) Circuit model of a reflector filter concept.

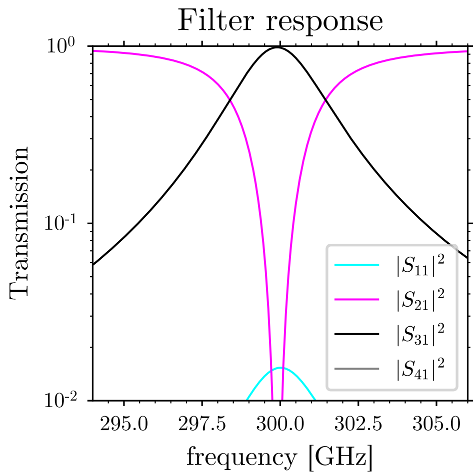

(b) Frequency response of a directional filter concept around its resonance frequency.

Figure 2.5: The directional filter concept

the two output ports. The coupling separation of $\lambda/4$ adds more spacing between filters, allowing for a better spacing of the detectors.

2.2 Filterbank Model

A filterbank is constructed using each filter type. An existing model is adapted by A. Pascual Laguna [16]. The filters are chained together in the manner shown in Figure 2.1. This example shows a filterbank with a spectral resolution of 100 and a bandwidth from 200 GHz to 400 GHz. The filters are ordered from the highest frequency to the lowest, which has two reasons. First, a filterbank spanning an octave or more will have the lowest frequency filters show spurious harmonics ($2f_0$, $3f_0$, $\cdots$). To combat this problem, the power available for these spurious harmonics is absorbed in the appropriate leading filters. Secondly, the highest frequency of the filterbank has the highest internal losses, therefore this signal is captured first before it is degraded further.

The calculation of the filterbank model is done by considering one pair of ports at a time, always using the input port as the source of incoming radiation. All the other ports are terminated with the appropriate loading. Using this method, the S-parameters of the full filterbank are determined. The result can be seen in Figure 2.6. The reflection coefficient, $|S_{11}|^2$, is shown in cyan. The transmission coefficient, $|S_{21}|^2$, is shown in magenta. In the top most figure an example filterbank using directional filters is shown, each colored peak is the response of one filter. For the subsequent plots, the envelope is taken of all filter responses. The individual filter responses for each filter type can be found in Appendix C

The envelope of the filterbank can be expressed as

$$\eta_{\text{env}}(f) = \max_i(|S_{i1}(f)|^2) \quad \forall f, \qquad i = 3, \ldots, N_{\text{filters}} + 2. \tag{2.4}$$

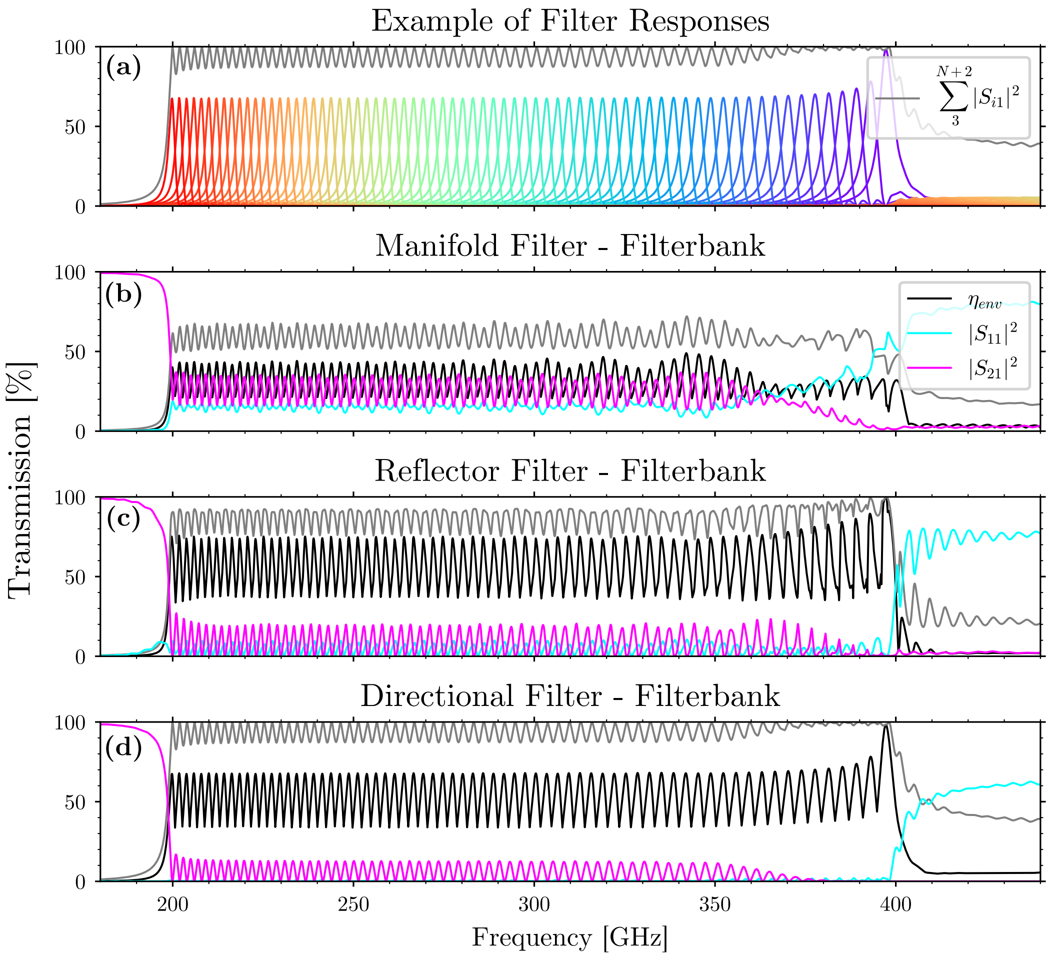

Figure 2.6: Circuit model of a filterbank using each filter type. Sub-figure **(a)** shows an example of individual filter responses in a filterbank. Subfigure **(b)-(d)** shows the response of a filterbank using each filter type. The responses of individual filters are replaced by the envelope for visual clarity.

The realized resonance frequency and Q-factor are found by determining the peak transmission and FWHM of the generated curves, as seen in sub-figure **(a)** from Figure 2.6. For each filter type, the realized Q-factor is shifted from the targeted Q-factor differently, which can be seen in the left plot of Figure 2.7. Embedding the filters in a filterbank causes interactions between them, resulting in shifting resonance frequencies and, more noticeably, altering Q-factors. Deviations of these parameters is unwanted for designing a filterbank.

On the one hand, a too high realized Q-factor will cause an under-sampling of the spectrum. This happens to the directional filter. This means that there are gaps in the coverage of the band of interest, i.e. there are regions where no filter has an in-band response.

On the other hand, a too low realized Q-factor will cause an over-sampling of the spectrum. This happens for the reflector filter and the manifold filter. The in-band embedded filter response is widened compared to the designed value of an isolated filter. The result is that filters overlap, reducing the power available to neighbouring filters. The total power captured might increase, but the response of individual filters is lower compared to the isolated filter case.

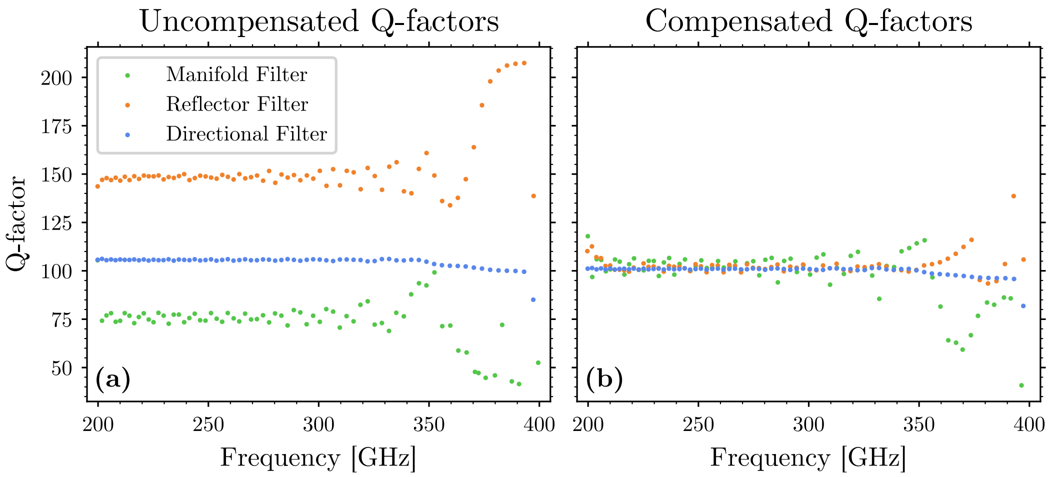

Figure 2.7: **(a)** Realized loaded Q-factor for each filter type. **(b)** Realized loaded Q-factor after the filter model is tuned to compensate for the Q-factor shift that is observed.

As a result, the Q-factors of the individual filters are biased in the model for each filter type to create a filterbank with the designed Q-factor. The manifold filter is biased with 1.15 times the targeted Q-factor, the reflector filter is biased with 0.75, and, the directional filter is biased with 0.95. The resulting Q-factors are shown in the right plot of Figure 2.7. A perfect sampling of the band of interested is realized. Using the compensated filterbanks, a fair comparison can be made for the performance of each filter type.

One thing to note is the manifold peak efficiency difference of the highest frequency filter, compared to the literature [16]. In the literature, the first, highest frequency filter has one of the best efficiencies, but for the filterbank presented here, this is not the case. The reason is the compensation of the Q-factors that we apply. The compensation widens the filters and creates unfavourable matching conditions for the first few filters, resulting in a low efficiency.

2.2.1 Comparison of Filter Concepts

Ultimately, the performance of the filterbank is governed by its impact on the integration time of the instrument. The line emission of a high-z galaxy is only detected in a reasonable time in a filter with a high response and low noise. Practically, this means that the most responsive filter dominates in a certain band when evaluating the filter performance. This is captured using two metrics.

The first metric is the in-band filter efficiency, which is a measure of the average efficiency within the FWHM of the filter. In terms of astronomical observations, the in-band filter efficiency shows how well a galaxy line emission signal couples to the detector. The formal definition of the in-band filter efficiency is

$$\eta_{f_i} = \frac{\int_{\Delta f_i} |S_{i1}(f)|^2 df}{\Delta f_i}. \tag{2.5}$$

The in-band filter efficiency of each filter is plotted in Figure 2.8 for each filter type. From this image, it is clear that both the reflector filter and the directional filter outperform the manifold filter.

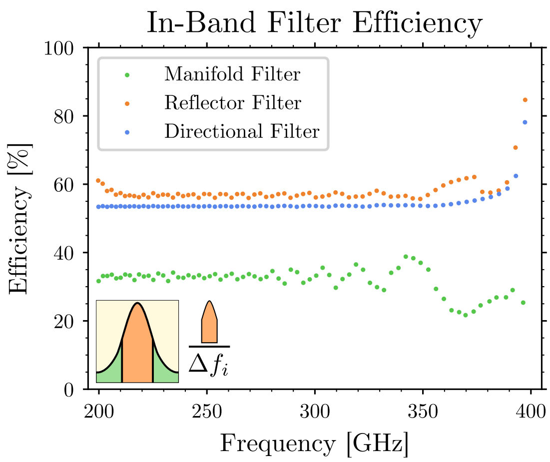

Figure 2.8: In-band filter efficiency for each filter type, evaluated in a filterbank configuration. The inset shows a graphical representation of Equation 2.5.

The second metric is the in-band fraction, which is a measure of what fraction of the total power impinging on a detector is in-band. The in-band fraction shows how much out-band excess noise is present when observing a signal in-band. A higher in-band fraction leads to quicker measurements of an on-sky source. The definition is given as

$$\eta_{IBF} = \frac{\int_{\Delta f_i} |S_{i1}(f)|^2 df}{\int_0^\infty |S_{i1}(f)|^2 df}. \tag{2.6}$$

Figure 2.9 shows the in-band fraction for each filter concept. The in-band fraction is similar for all filter types. The reflector filter has a slightly higher in-band fraction, which can be explained by the slightly sharper sideband roll-off, as can be seen in Figure 2.4b.

All filter concepts can be considered first-order filters, so their decadal roll-off is similar. A higher order filter will be able to improve this metric. This is interesting for follow-up research, since this has the potential to further improve the performance of the filterbank. The biggest downside of adding more filtering elements is the increased dielectric losses, this will grow with the number of resonators used.

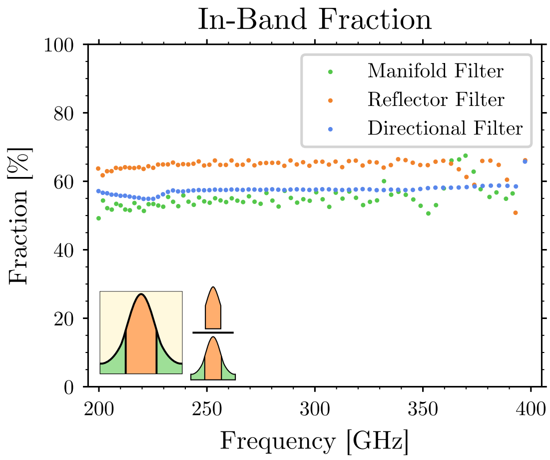

Figure 2.9: In-band fraction of each filter type. The inset shows a graphical representation of Equation 2.6.

2.3 Conclusion

All-in-all, the two newly introduced filter concepts that have been investigated show a significant performance improvement against the manifold filter concept. However, between the directional filter and the reflector filter concepts, there is no clear advantage for either one. The biggest remaining question for these concepts is their robustness against losses and tolerances in the fabrication processes. These questions will be addressed in the next chapter.

3

Modelling Tolerances and Losses of a Filterbank Spectrometer

The circuit model we have used has assumed that we can realize the proposed circuits ideally, and without losses. In this chapter, we evaluate the proposed coherent-phase filters with a more realistic model. Firstly, a circuit model subject to tolerances is evaluated. The tolerances are based on measurements done on a similar on-chip filterbank spectrometer. They are applied to the model by adding variances to the key design parameters of the comprising filters, namely it resonance frequency (f_i) and its loaded Q-factor (Q_{L}). Increasingly intense variances are applied to the model to show the deteriorating function of the filterbank for each filter type.

Secondly, losses are added to the circuit model. Ohmic losses in the circuit model are zero, since the device is assumed to be superconducting. However, two sources of losses still exist. Firstly, losses can occur by radiation [24], [25], but this is strongly reduced by the use of microstrip structures near the filtering elements [16]. Therefore, radiation losses are not considered in the circuit model. Dielectric losses are the main contributor to the losses in our system, and are strongest where the electromagnetic field produced by the signals is strongest. The electromagnetic field is strongest in the resonators, therefore, losses in the circuit model are only applied to the resonators.

3.1 Variances in the Filterbank Model

Understanding how a filterbank is impacted by tolerances in its fabrication will allow us to choose the most robust filter type and get a better estimate of its performance. The method to incorporate these tolerances is by adding variances to Q_{L} and f_i of individual filters. An example of variances applied to the filters of a filterbank can be seen in Figure 3.1. In Appendix D an example of a filterbank subject to variance is given for each filter type.

These variances are modelled after measurements of a similar chip. There are many potential causes for these variances (e.g., in the etching, in the material properties, in the thickness and in the design). The exact contribution of all these causes to the variances has not been determined, and it is very difficult, if not impossible, to do so accurately for use in a model. Therefore, an approach independent of the individual contributions is desirable.

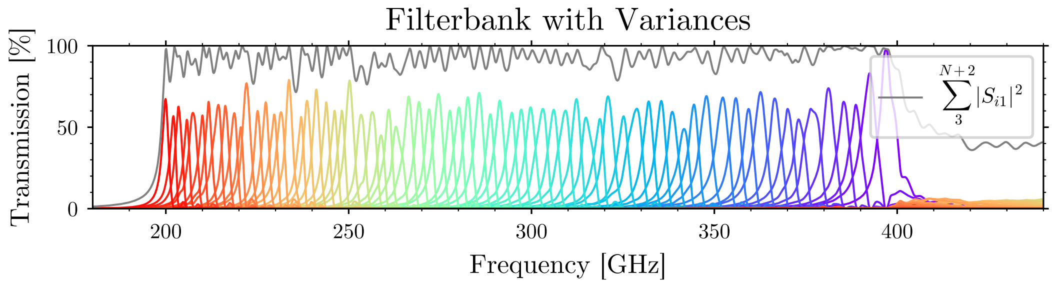

Figure 3.1: A circuit model of a filterbank showing variances applied to individual filters. Directional filters are used for this example with an f_i variance of 20% around its nominal value, and a Q_L variance of 10% around its nominal value. The definitions of the errors used to calculate the variance are given by Equations 3.1 and 3.2.

3.1.1 Method

Our proposed method for incorporating the variances in the model is as follows. A random perturbation is added to the designed nominal value of Q_L and f_i of each filter in the model, based on a normal distribution. The normal distribution is calculated using the following errors. The error of the resonance frequency, normalized to the designed spectral width, is defined as

$$e_{f_i} = \frac{f_i^{\text{meas.}} - f_i}{\Delta f_i}, \qquad \text{where } \Delta f_i = \frac{f_i}{Q_\mathrm{L}}. \tag{3.1}$$

The error of the loaded Q-factor is defined as

$$e_{Q_\mathrm{L}} = \frac{Q_{\mathrm{L},i}^{\text{meas.}} - Q_\mathrm{L}}{Q_\mathrm{L}}. \tag{3.2}$$

Measurements performed on a similar chip by K. Karatsu (private communications, 15 October 2021) are used to find a set of representative errors of Q_L and f_i for a manufactured device, from which a normal distribution is constructed. These measurements were performed for a filterbank with a loaded Q-factor of 500. Therefore, for Q_L equalling 100 in our case, the variances are divided by five, which follows from the Q_L dependence in Equations 3.1 and 3.2.

Since we do not know the physical variances for individual components, we choose to apply the variances at the resonator level, and not at the component level. Our abstraction is still relevant, however, since the result of the component level tolerances is a resonator with an imperfect Q_L and f_i. Furthermore, any offsets in the normal distribution of the errors of Q_L and f_i are not applied in the model. These are systematic errors which are hard to control from chip to chip, and they impact the performance of a filterbank less than relative variances from filter to filter.

Note that the Reflector filter and the Directional filter have multiple resonators (the reflector section is considered a resonator). In the model, each resonator within a filter will get a different error applied. This choice is based on the measurements of the variances. These measurements show that physically close filters still show large variances between them. Meaning that the dominant variances that act on the resonators are location independent and uncorrelated from each other. This implies that for our more complex filter designs the resonators can be shifted in their Q_{L} and f_i independently, and this is reflected in the model by applying the errors at resonator level.

Efficiency metrics are needed to evaluate the performance of the filterbank, with variances, and for each filter type. In Section 2.2.1 two metrics were introduced to compare filter concepts, namely, the in-band filter efficiency and the in-band fraction. The in-band fraction is not very useful for the current comparison, since it was established that this metric was similar for all filter types due to all filters having the same filter order.

As a better alternative to the in-band filter efficiency, the average envelope efficiency is introduced. It is a filterbank wide metric which better captures the on-sky performance of a chip with tolerances. The average envelope efficiency is calculated by finding the transfer efficiency of the most responsive filter for each frequency across the full bandwidth of the spectrometer, i.e. the envelope (see Equation 2.4), and taking the average. It is formally defined as

$$\overline{\eta_{\mathrm{env}}} = \frac{\displaystyle\int_{f_{\mathrm{min}}}^{f_{\mathrm{max}}} \eta_{\mathrm{env}}\, df}{B}, \tag{3.3}$$

where B, f_{min} and f_{max} are given by Equation 1.3.

The average envelope efficiency is equal to the average of the in-band filter efficiency when the filters are perfectly spaced. But when variances are introduced to the circuit model, the in-band filter efficiency overestimates the efficiency of the filterbank. With variances, filters can partially share the same bandwidth or leave gaps. In the overlapped bandwidth, two filters will efficiently couple to an on-sky source, but no extra information is gained. In the gaps, the low efficiency is not recorded, since it does not fall in-band of any filter. So, to make sure an accurate efficiency of the full bandwidth is recorded, the average envelope efficiency is used. An example of the $\overline{\eta_{\mathrm{env}}}$ can be seen in Figure 3.2.

The final metric that is introduced is the usable spectral fraction (USF). The USF is the fraction of the envelope that is above $(\sqrt{2})^{-1}$ $(= -1.5\,\mathrm{dB})$ times the average envelope efficiency. The USF is defined as

$$\mathrm{USF} = \frac{N_{\mathrm{env}}\left(\eta_{\mathrm{env}} > \dfrac{\overline{\eta_{\mathrm{env}}}}{\sqrt{2}}\right)}{N_{\mathrm{env}}}, \tag{3.4}$$

where N_{env} is the number of data points in η_{env}.

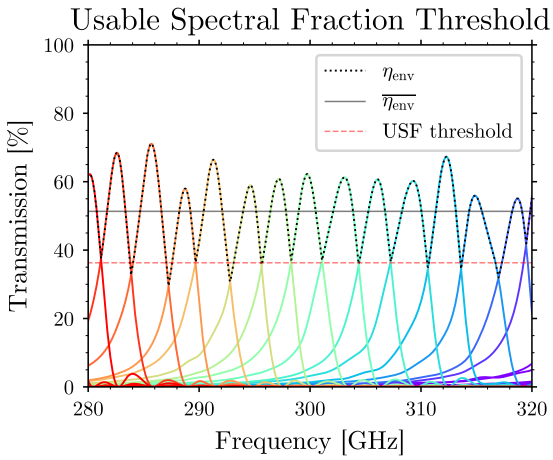

Figure 3.2: Illustration of how the average envelope efficiency and usable spectral fraction are calculated for a filterbank.

This threshold is shown as the dashed red line in Figure 3.2 and is chosen for three reasons. Firstly, this threshold corresponds to a dynamic range of two in the filterbank efficiency. Considering that the peak efficiency is estimated to lie at $\overline{\eta_{\text{env}}} \cdot \sqrt{2}$ $(= +1.5\,\text{dB})$ on average, the dynamic range of the filterbank is around 3 dB. In other words, the lower end of the usable spectral fraction is half as efficient as the peaks. Secondly, this threshold is sensitive to small filter variances, allowing a high quality comparison for a large range of Q_{L} variances and f_i variances. Lastly, for a perfectly spaced filterbank, this metric will be equal to the in-band filter efficiency.

3.1.2 Results

The variances are incorporated in the model as described by the method, and the model is run for several combinations of Q_{L} variances and f_i variances for each filter type. In Table 3.1 all the combinations that were run through the model are listed. For each combination and filter type, the model is run twenty times. In Figure 3.3 histograms of the realized f_i and Q_{L} parameters are shown for each filter type.

The histograms differ from the input f_i and Q_{L} variances. Each resonator gets a defined variance that is drawn from the input distribution, but intra-filter interactions for the directional filter and reflector filter lead to the final variance observed to be different. These interactions are not equally strong for each filter type, and can explain

	Ideal	Measured	Extreme
σ_{f_i}	0.00	0.12	0.30
$\sigma_{Q_{\text{L}}}$	0.00	0.07	0.15

Table 3.1: Variance settings used for modelling the tolerances on the chip.

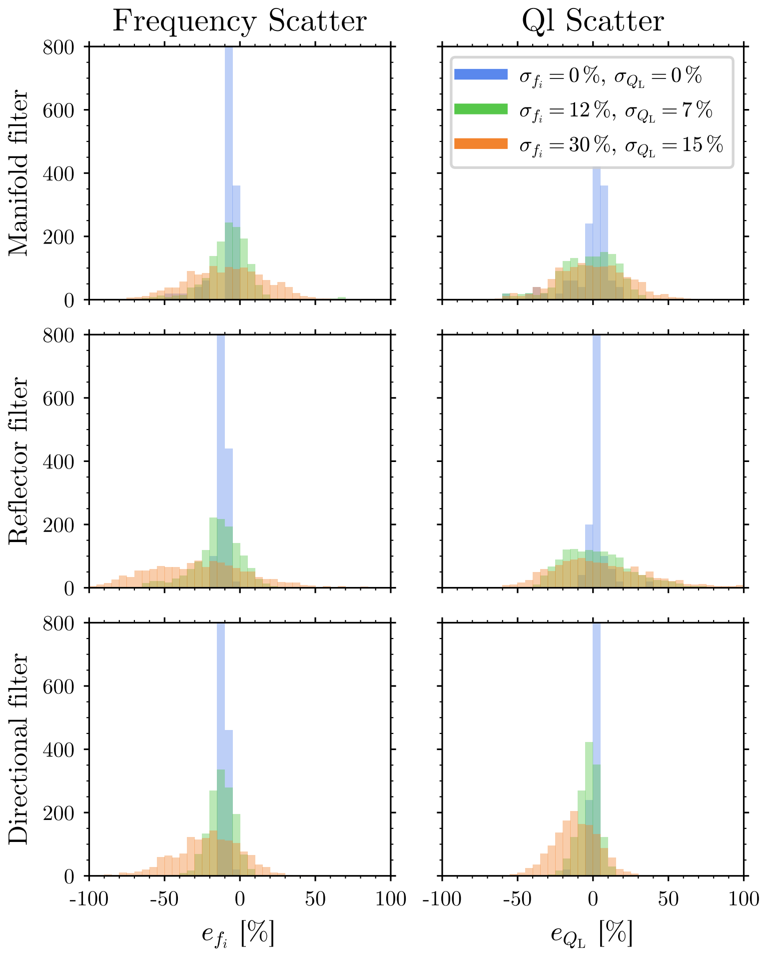

Figure 3.3: Histograms of each filter type showing the distribution of realized errors due to an introduced variance given by Table 3.1. Twenty filterbanks are simulated with 70 filters each, resulting in a dataset of 1400 filters for each combination of filter type and variance applied.

the worsening variance of the Reflector filter and the improved variance of the Directional filter.

Another reason for the difference is due to neighbouring filter interactions in the filterbank. The variances in the filters cause them to overlap or leave gaps. If two filters overlap significantly, they change the loading at that frequency. In most cases, the first filter receives most of the incoming energy, leaving little for the overlapping filter. This causes the second filter to have a forced sharper roll-off due to less energy being available, which skews the Q-factor and shifts the resonance frequency.

The f_i and Q_L of a filter are correlated, making it difficult to state definitive conclusions on the reasons for their variances. If the resonance frequency shifts down, the physical capacitor component should increase to keep Q_L equal, which follows from Equation 2.1.

The physical capacitor is constant and cannot change its geometry, therefore a downshift in f_i will result in an up-shift in Q_L, and vice versa. Alternatively, a change in Q_L first will shift f_i. If Q_L decreases from its designed for value, the zero phase loading of the resonator shifts to a higher f_i (for a constant resonator length), due to less loading. The reverse, an increase in Q_L will downshift f_i. In summary, the realized f_i and Q_L have an inverse relationship.

It is observed that the mean of the resonance frequency is shifted down for all filter types. It is believed that the ordering of the filters is the cause. The higher frequency filters cause the absorption of part of the signal, and the next filter is skewed to a lower frequency. For higher variances, the closest higher frequency filter is likely to overlap more with the next filter, and that will strengthen the skewing effect.

Figure 3.4 shows boxplots of the average envelope efficiency and the usable spectral fraction for each filter type for the variances of Table 3.1 applied to the model.

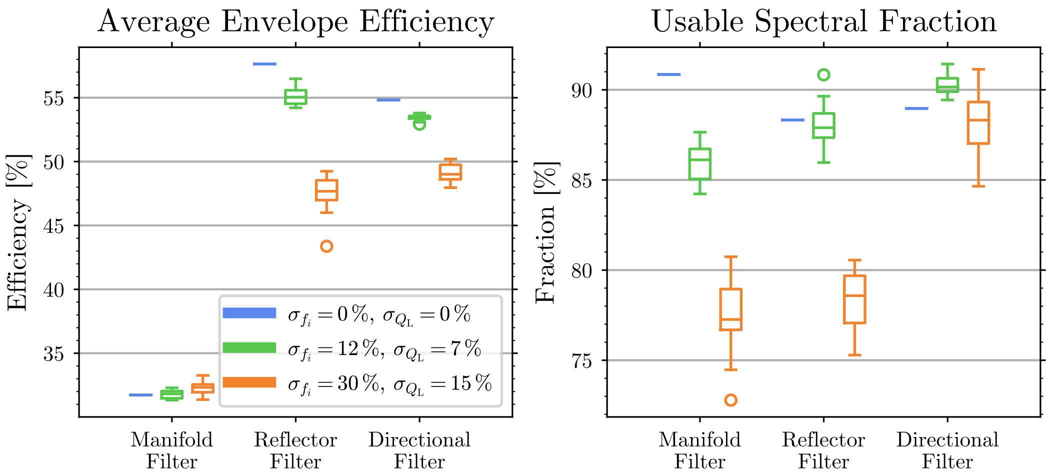

Figure 3.4: Boxplots average envelope efficiency and usable spectral fraction. The applied variances are given by Table 3.1.

First, the average envelope efficiency is evaluated. The non-variate case is equal to the efficiency observed in Section 2.2.1. The manifold filter is not affected by the variances. The reflector filter shows the largest decrease in average envelope efficiency, which can be attributed to the reflector sections variating independently in regard to their filter sections. The loading of the filter section is not as good, and the performance will approach that of the manifold filter. The directional filter has the most gradual decrease in performance. It is expected that for variances worse than the case presented here, the directional filter will have the best efficiency.

Second, the usable spectral fraction is evaluated. The perfectly designed filterbanks show a similar usable spectral fraction of around 90%. For moderate variances, the reflector filter has an equal performance compared to the no variance case. Once the variance becomes large enough, the reflections caused by the variating reflector sections cause larger gaps in the USF. The directional filters manage to stay as a coherent filter unit longer, which results in a high USF for all variances applied.

All in all, the directional filter is the most robust design against tolerances. Firstly, the histograms of the realized parameters show the least variance compared to the other filter types. Furthermore, the rate of decline of the average envelope efficiency is the slowest of all the filter types. Lastly, the coherence of the filter units lead to a high usable fraction for significant variances. These simulations of a realistically fabricated filterbank of this filter type suggest the most robust on-sky performance. Looking towards the near future, filterbanks that target a higher spectral resolution, and therefore higher Q-factor, will benefit more significantly from this filter design.

3.2 Losses in the Filterbank Model

Before a final conclusion can be made on the filter type that will be fabricated into a test chip, a loss analysis is performed. The dielectric losses of the substrate are the main source of losses in our system. The dielectric losses in the system are applied to the resonators, since in these sections the electromagnetic field is strongest. We add the losses to the resonators by using a complex propagation constant $\gamma = \alpha + i\beta$ for the resonator transmission lines, where the real part α is the attenuation constant and the imaginary part β is the propagation constant. The internal quality factor is used for defining the attenuation constant of the resonator $\alpha = \beta/2Q_\mathrm{i}$ [18].

Figure 3.5 shows a boxplot of filterbank simulations with and without losses. The reflector filter and the directional filter both show a similar decrease in efficiency due to resonator loses. Based on this analysis, no clear advantage is seen for either filter type.

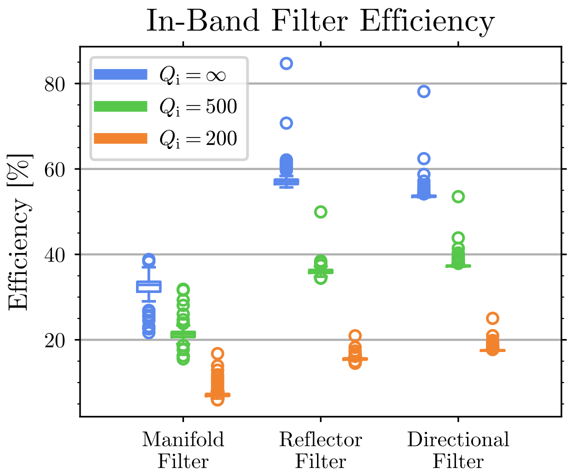

Figure 3.5: Simulation of a filterbank for a number of internal quality factors of the resonators.

3.3 Conclusion

In conclusion, the directional filter is the filter type that is most robust against fabrication tolerances and shows no extra losses compared to the other designs. The model that is used allows for a good assessment of these effects, without the need for all sources of tolerances to be known. The model can help us predict the performance of the chip ahead of time. These models can be used in a simulation pipeline of on-chip spectrometer instruments to evaluate the full-stack performance.

The directional filter concept is chosen to be fabricated in the test chip.

4

Chip Design

In this chapter, a filter design for the directional filter concept is proposed. A. Pascual Laguna et al. [16] have shown that microstrip filterbanks are required to achieve the wideband coupling performance we desire. A drawback of using microstrip technology instead of co-planar technology is the need for a deposited dielectric between the conductor and ground plane, which are typically more lossy than crystalline substrates. Recent developments by B. Buijtendorp et al. in the THz sensing group have established silicon carbide (SiC) as a suitable low loss material [26].

The realized filter design that is proposed in this chapter uses a vertical coupling structure. The capacitive coupling is achieved by overlapping two microstrip lines, which are separated by a SiC dielectric. This structure is best suited for low spectral resolution devices, as these couplers are quite strong. We expect this coupling geometry to suffer less from fabrication tolerances compared to a planar coupling structure, where the edge-to-edge coupling is hard to control (D. Thoen, private communication). In Section 4.1, we will detail the reasoning behind our choice. Here, the filter design is also validated using a SONNET model.

A test chip is fabricated to confirm the models and simulations. This test chip will have a filterbank and a number of isolated filters, to judge the performance of the filter design in both cases. In Section 4.3.1 the design of the test chip is explained.

Finally, the fabrication process is described in Section 4.3.2.

4.1 Filter Design

The directional filter concept in Section 2.1.4 is used to make a physically realizable filter design. For our design, we target a spectral resolution, or loaded Q-factor, of $R = 100$. This is done for two reasons. The first is that we would like to minimize the impact of losses on both the spectral resolution and the coupling efficiency. The internal losses of the resonator (Q_i) influences the loaded Q_l according to Equation 2.2. If we design for $Q_l \ll Q_i$, the filters become dominated by the Q_c term for determining Q_l. By choosing a lower target spectral resolution, we can prevent excessive losses that could prohibit proper characterization of the filters. The second reason is that a lower spectral resolution will require fewer filters to cover an octave band, while still having enough filters to study the effects of a filterbank. This also has the effect of suppression of the relative variances that are present due to tolerances in the fabrication.

Figure 4.1 shows the filter design that is used to implement the directional filter concept. The resonators are oriented vertically in the figure. The THz-line and the detector line are connected at the top and at the bottom, respectively. All relevant dimensions of the filter are marked.

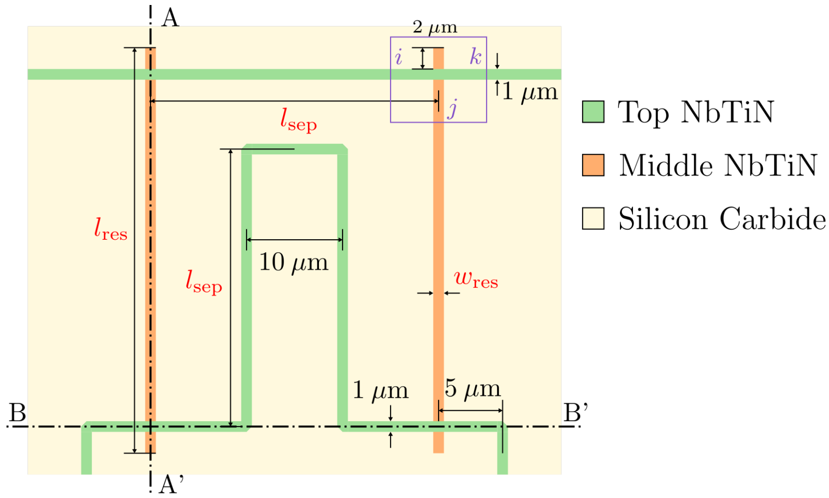

Figure 4.1: Filter design of a directional filter. A vertical coupling structure is used. A-A' and B-B' mark the cross-sections shown in Figure 4.2. The purple box indicates the structure that was simulated for finding the coupling strength.

The structure is characterized by a number of fixed material parameters (ε_r, L_k) and several fixed geometry parameters (SiC thickness, w_{THz}, w_{det}). The frequency dependent geometry of the filterbank is defined by three parameters: The length of the resonators (l_{res}), the width of the resonators (w_{res}) and the quarter lambda separation distance (l_{sep}).

For the structure to operate efficiently, all ports should be matched with the correct impedance (see Section 2.1.4). The matched load is realized with a lossy transmission line whose length is chosen so to absorb 95% of the input power. The output of the filter (ports 3 and 4) is connected to the hybrid section of the MKID, which has a characteristic impedance of 71 Ohm. The output is the top-layer microstrip with a thickness of the SiC dielectric of 300 nm and an epsilon effective[1] (ε_{eff}) of 42.9. A 1 μm wide microstrip has a characteristic impedance of 72.8 Ohm, which is a good match to the MKID. The THz-line is made the same width to keep the symmetry and provide a good match to the antenna CPW feed. A summary of the design specifications is given in Table 4.1.

[1]SONNET gives the ε_{eff} with the effects of kinetic inductance included. Physically, this is not correct, but the ε_{eff} given is a useful parameter for determining the phase velocity in the transmission line.

Materials		
ε_{r}	SiC	7.7
L_{k}	NbTiN 100 nm	1.18 H
	NbTiN ground	0.65 H
Geometries		
t_{SiC}	bottom	200 nm
	top	100 nm
l_{sep}	$\lambda/4$ separation	30.4 µm to 60.5 µm
Resonator line		
l_{res}		43.1 µm to 92.3 µm
w_{res}		0.8 µm to 3.1 µm
Z_0		70.7 Ω to 22.2 Ω
$\varepsilon_{\mathrm{eff}}$		65.5 to 60.5
Detector & THz-line		
w_{THz}		1 µm
Z_0		72.8 Ω
$\varepsilon_{\mathrm{eff}}$		42.9

Table 4.1: Fixed and variable parameters for the directional filter design.

4.1.1 Vertically stacked coupling structure

In previously developed chips, co-planar microstrip coupling structures were used. A co-planar structure is limited by the alignment accuracy and the minimal feature resolution of the lithography in the horizontal plane. The tolerances cause the center frequencies and pass-bands to vary wildly within a single filterbank. These tolerances are in the range of hundreds of nanometers for optical processes, and tens of nanometers for electron-beam patterning. For on-chip spectrometers with a spectral resolution greater than $R = 500$, it becomes a significant problem. In that case, the fabrication tolerances exceed the accuracy needed to properly space the resonances and maintain a constant Q_l over the filterbank, leading to filter properties shifting by many filter widths.

Three-dimensional fringe-field coupling effects are hard to model in commonly used software packages, due to unpredictable material properties, alignment accuracies, fabrication variances and inaccuracies in the computer models. The fringe-field coupling effects are exacerbated by unpredictable over-etch rates in the supporting dielectric, which influence the electric fields that couple across the gap. On the other hand, three-dimensional solvers such as CST Microwave Studio are less accurate than SONNET in predicting the resonance frequency of superconducting circuits [17], [27].

The alternative proposed here is a vertical coupling structure between two microstrip layers separated by a thin dielectric. A cross-section of such a coupling structure is shown in Figure 4.2. The main parameters that would govern the coupling strength are the area of the overlapping microstrip lines and the dielectric thickness. Current microchip fabrication techniques can accurately control the thickness of a deposited dielectric layer within tens of nanometers. Furthermore, this dimension is more easily managed across the filterbank, reducing relative errors. Since these structures are typically wide and not thick, the effect of fringe-fields is reduced. All in all, vertical coupling structures can be more accurately modelled. The caveat is a more complex fabrication process of the chip, since two additional layers (the separating dielectric layer and the top metal layer) need to be deposited to form vertical coupling structures compared to planar devices.

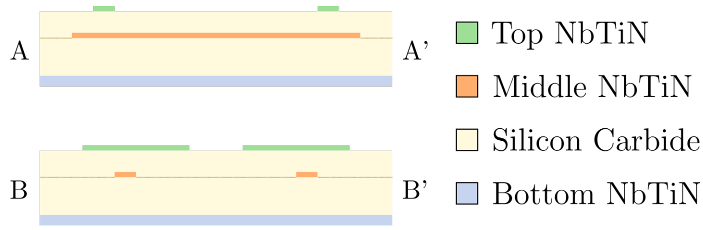

Figure 4.2: Cross-section of the directional filter design. This figure shows clearly how the vertical coupling is achieved.

The vertical coupling structure reduces the coupling footprint needed, compared to a planar design. This helps to space the coupling structures at $\lambda/4$ without the ends of the couplers interfering with each other, thereby allowing a single-sided filterbank. The $3\lambda/4$ section is meandered inward to reduce the overall footprint.

The area of the coupling capacitance is determined by the widths of the resonator and THz/detector line that are overlapped. Since the width of the THz/detector line is already defined, the total area of the coupler is solely determined by the width of the resonator (w_{res}). The coupling area on both sides of the resonator is made equal to simplify the filter design procedure. The THz-line and the detector line need to have the same width to satisfy this condition.

The width of the resonator is constantly changing to match the coupling strength, but this also means that the characteristic impedance and $\varepsilon_{\mathrm{eff}}$ are continuously changing. In Figure 4.3, These parameters are modelled across a number of realistic resonator widths to allow for an accurate design across all frequencies. These parameters form the basis for the coupling strength calculation.

The coupling strength that matches the coupling Q_{c} needs to be determined for each frequency. The Q_{c} of a fixed area changes with frequency, so the area needs to be adjusted across the band to keep Q_{c} constant. The coupling junction is simulated across the full filterbank frequency range for a number of realistic w_{res} values. The simulated coupling junction is marked with a purple box in Figure 4.1.

The optimal coupling strength for the desired Q_c is

$$|S_{ij}|^2 = \frac{2\pi}{2Q_c}. \tag{4.1}$$

This formula is derived in Appendix B based on the energy leaking definition of Q_L in Equation 2.1.

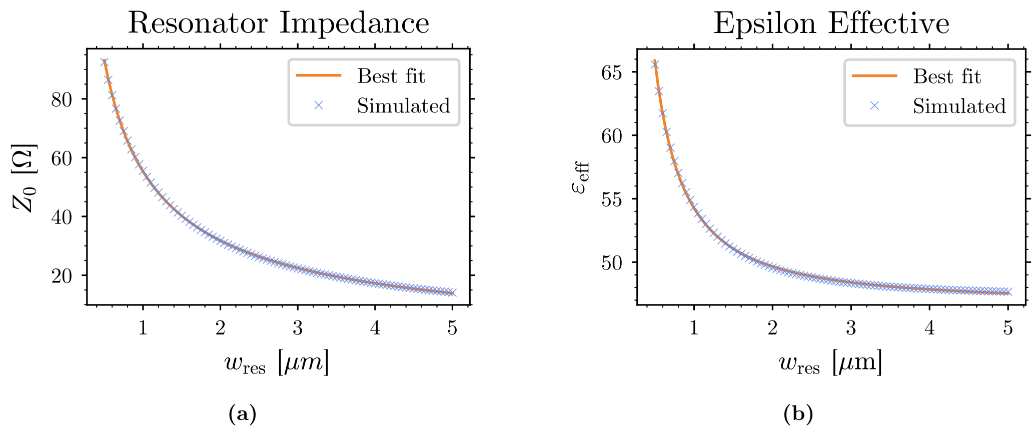

Figure 4.3: Simulation of the resonator impedance and ε_{eff} for different resonator widths.

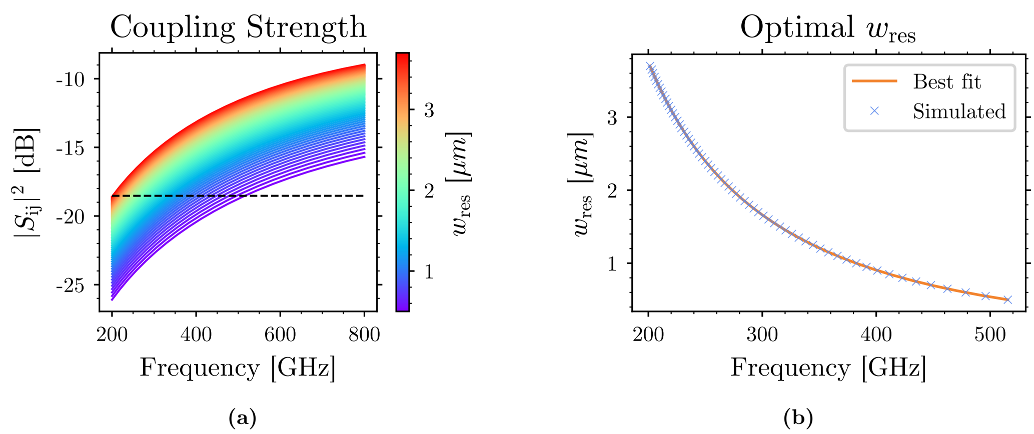

Figure 4.4: Optimal resonator width for a filterbank spanning 200 to 400 GHz and with a spectral resolution of 100.

If we assume a lossless device and equal coupling for both sides of the resonators to simplify the calculation, we can use: $Q_c = 2Q_l$. Given the spectral resolution (R) design specification, we can find the coupling strength needed at that frequency. For $R = Q_l = 110$, the coupling strength is $|S_{ij}|^2 = -18.5$ [dB]. In Figure 4.4a, the simulations of a coupler with different resonator widths can be seen. The intersection with the dashed line at -18.5 [dB] is the optimal width at that frequency. The frequency and width of the resonator is collected for each intersection. Figure 4.4b shows the optimal width across the desired frequency. A fit is applied to interpolate between the data points.

Finally, to complete the filter design, the loaded resonator length and the $\lambda/4$ separation length need to be determined at the desired resonance frequency f_0. The resonator length of a loaded resonator is calculated using the model of Section 4.1. The propagation constant of the THz/MKID line is used to find the length needed for a phase change of $\lambda/4$ and $3\lambda/4$.

4.1.2 Filter Simulation Compared to Model

A section of three contiguous filters is simulated in SONNET and is compared to the model. Three filter sections are connected with a $\lambda/4$ spacing. The geometry that was drawn in SONNET is equal to the geometry in Figure 4.1. The variable parameters are given by the method in Section 4.1.1. Only three filters are simulated to keep a reasonable simulation time.

In Figure 4.5 the results can be seen. Compared to the model, the resonance frequency of the filters is shifted upwards. This effect is partly due to the grid resolution used in SONNET, which was confirmed by running a single filter with a finer grid. The finer grid would result in a more accurate result, at the cost of a longer simulation time.

Furthermore, as seen from the filter design in Figure 4.1, the couplers are not located exactly at the ends of the resonators. This might have two effects. First, the effective length of the resonator might be slightly shorter, increasing the resonance frequency. Second, the metallic structure of the THz-line and coupler might affect the propagation constant around the resonator, which might also affect the resonance frequency. These two effects can account for the residual error present in the simulations.

All in all, The simulations are in good agreement with the model. The peak efficiency of the model has a bit lower efficiency than the model, but this will not hurt the performance of the filterbank. The simulation time of approximately four hours is a big loss of time compared to the circuit model, which runs in approximately thirty seconds. The model therefore is the ideal tool to synthesize many filterbank configurations. It is also the ideal platform to test new filter types, given that it can be fabricated.

4.2 MKID Design

The MKID is connected to the filter as shown in Figure 4.6. The MKID resonator is constructed using four sections. On the left of the figure, the short-circuited hybrid section is connected to the filter and is long enough to absorb the input power that emerges from the filter. There, it passes through the lower part of the filter on the top wire, whose length is determined by the filter design. Next is the second hybrid section, whose length is also long enough to absorb the input power. Finally, the wide NbTiN section extends from this second hybrid section and is coupled to the readout at its end.

These sections have different impedances and propagation speeds, therefore constructing an analytical expression for the wide NbTiN section length for a given resonance frequency is difficult. The resonance is found using microwave techniques using the known

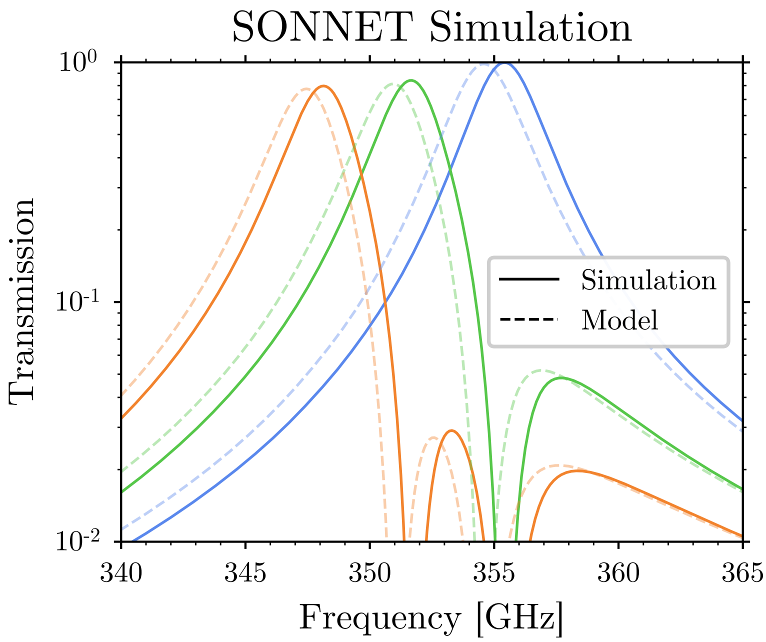

Figure 4.5: Simulation of three contiguous filters compared to a simulation of three filters with the same dimensions. There is a good agreement between the model and the simulation.

impedances and propagation constants of each section. The final section, the NbTiN CPW line, is tuned in length to find the desired resonance frequency.

A difficulty for practically implementing this is the shuffling of readout frequencies and filter frequencies. Depending on how the readout frequencies are shuffled, a different THz frequency filter might be attached to an MKID resonator with a certain frequency, say 5GHz. The lower section of the filter that is part of the MKID changes length according to the THz frequency.

Normally, the manufacturing risk of the MKIDs is minimized by setting a fixed ratio between the hybrid CPW line and NbTiN CPW line. Any fabrication errors in a single step, such as etching the aluminium, will cause a proportional resonance frequency error in each MKID. The relative frequency spacing is better preserved by using a fixed ratio. For the directional filter, the lower section of the filter has a variable length, which is not determined by the readout frequency but by the THz filter resonance frequency.

The geometry of the hybrid CPW section of the MKID largely determines the response of the MKID and is optimized to match the impedance of the filter, but this constrains the MKID design. The aluminium width and thickness of the lossy hybrid section is used to match the impedance between the filter and the MKID at THz frequencies. If the return path of the reflection is long enough, all power will be absorbed. The load seen from this hybrid section will be the characteristic impedance of the CPW, and this connection is made to match. The aluminium sections must be made long enough to

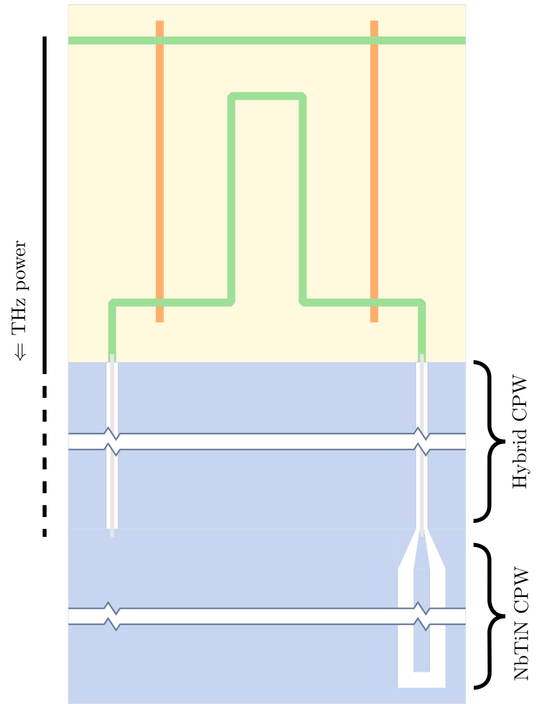

Figure 4.6: Illustration of the MKID connection to the filter. Note how the lower part of the filter is part of the MKID.

absorb most THz power before it can be connected to something else. However, we cannot make the lines too long, because this would make a too large portion of the MKID resonator out of aluminium, which adds too much noise to the MKID detector.

The threshold for the percentage of absorbed THz power is set at 95%. Next, the aluminium section is designed with the correct impedance matching and absorption rate to reach this absorption at or under a certain length. This maximum length is set as 25% of the total resonator length. An aluminium thickness of 30 nm is assumed. Since the filter structure needs a proper load on both arms of the detector line, two aluminium sections are needed that can absorb the signal in half the total fraction available (which is 12.5%).

A section of hybrid CPW line is simulated using SONNET using the method described in [27]. The aluminium of the hybrid CPW is a lossy material at THz frequencies, since it is not superconducting. The lossy transmission of the CPW line can be described using a complex propagation constant, $k = k_0\sqrt{\varepsilon_{\mathrm{eff}}} = \beta - j\alpha$. Here, α is the attenuation constant, and β is the phase constant. α describes the attenuation per unit length, and we would like to find this value using SONNET.

In SONNET, the losses in the system are captured in the $\varepsilon_{\mathrm{eff}}$ parameter. Using this data, α can be found by solving the following system of equations:

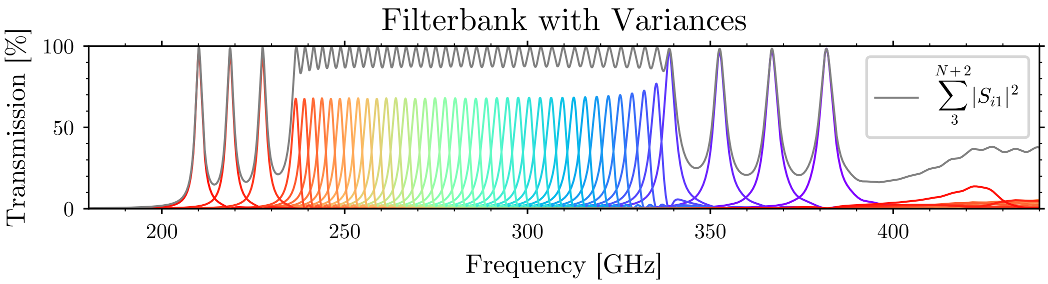

Figure 4.7: Simulation of the filterbank implemented on the test chip. Note the isolated filters before and after the densely sampled section, which are used to characterize the isolated filter response in the measurements.

$$\mathrm{Re}\{\varepsilon_{\mathrm{eff}}\} = \frac{\beta^2 - \alpha^2}{k_0^2}, \tag{4.2}$$

$$\mathrm{Im}\{\varepsilon_{\mathrm{eff}}\} = \frac{-2\alpha\beta}{k_0^2}. \tag{4.3}$$

It is found that, for a thickness of 30 nm for the aluminium, a CPW line of 1-1-1 micrometer is needed to achieve 95% attenuation in under 12.5% of the resonator length.

4.3 Test Chip

The filter design as shown above will be placed on a test-chip. The test-chip will be based on the chip design for DESHIMA 2.0 [28]. In Section 4.3.1 the design specifications of the filterbank is presented. In Section 4.3.2 the fabrication is described in detail. Finally, in Section 4.3.3 the problem of over-etching and step coverage is explained. This is a common problem for fabrication with many layers, which is the case for this test chip design.

4.3.1 Design

Anticipating the measurement setup, we design the test-chip filterbank between 200-400 GHz. This frequency range allows us to use the cryostat and measurement setup that is present at the TU Delft, without changing any of the optical filters. The center frequencies of the filters in the filterbank are calculated using the model of Chapter 2,

To evaluate the filter performance and efficiency accurately, a number of spectrally isolated filters are placed at the ends of the filterbank. These filters are spaced in frequency by several filter widths. Practically, this is done by not patterning the resonators of the neighbouring filters and also removing the aluminium sections of the corresponding neighbouring MKIDs. The simulated filterbank of the test chip can be seen in Figure 4.7.

The test-chip will have a leaky wave antenna on a silicon nitride (SiN) membrane that couples the energy to a CPW. This CPW is coupled to a microstrip on the SiC, which is the start of the filterbank. Next are the filters, ordered from the highest frequency to the lowest frequency. A quarter-wave transmission line MKID is connected to each filter, with their readout frequencies shuffled compared to their THz filter frequencies. This prevents neighbouring MKIDs from having similar resonance frequencies and exciting each other. Finally, the readout line is capacitively coupled to the MKIDs.

Unlike previous designs, all the MKIDs can be placed on the same side of the THz line. This is better, because slowly varying manufacturing tolerances that cause relative readout frequency shifts between MKIDs are minimized. As a result, MKID readout frequencies will have a smaller relative shift between them. This allows a larger total number of MKIDs that can be read out using one multiplexed coax-cable, and makes a higher detector yield more likely [29].

4.3.2 Fabrication

The fabrication starts with a crystalline silicon wafer with a thickness of 390 μm. A 200 nm thick NbTiN layer is deposited. This layer is then patterned and etched to form the ground plane of the filterbank. The first layer of SiC with a thickness of 200 nm is deposited to form the support for the resonators. A 100 nm thick layer of NbTiN is deposited. This layer is patterned using electron-beam lithography to form the resonators. Next, the resonators are covered by a layer of SiC with a thickness of 100 nm, which form the support structures for the coupling structures of the THz line and the MKID. The top layer of NbTiN has a thickness of 100 nm and is patterned using a combination of e-beam lithography and optical lithography. This step forms the CPW lines connecting to the antenna, MKID and absorber terminating the THz-line. A layer of polyimide is deposited. This ensures step coverage at the transitions from CPW to microstrip at the THz-line and at the outputs of the filters to the MKIDs. It also provides support for the bridges balancing the grounds of the CPW, and provides a bridge for aluminium center line connections of the hybrid CPW sections on the NbTiN ground plane. Next is the deposition of a 40 nm thick aluminium layer. This layer is defined using a combination of optical and e-beam lithography. On the backside of the wafer, a 40 nm thick β-Ta absorption layer is deposited. Finally, KOH etching of the Si wafer is done to form the membrane of the antenna [30]. This process is shown in a cartoon in Figure 4.8.

4.3.3 Over-Etching

Each layer that is deposited needs to be patterned and stripped away to define the layer according to the mask. The wafer is exposed to a corrosive substance that etches the exposed layer at a certain rate, determined by the material properties. This corrosive substance is often not perfectly selective to a single material, and once the layer is corroded away will start to etch into the underlying layer. This is called over-etching.

In any microchip fabrication process, over-etching can be expected. The etching process is kept running slightly longer than necessary to guarantee that all excess material of the exposed layer is removed. A common percentage used for the over-etch is to etch 10% longer than the end point detection time. Adding this safeguard is especially crucial for conductive layers, because accidental residual material will cause unwanted electrical

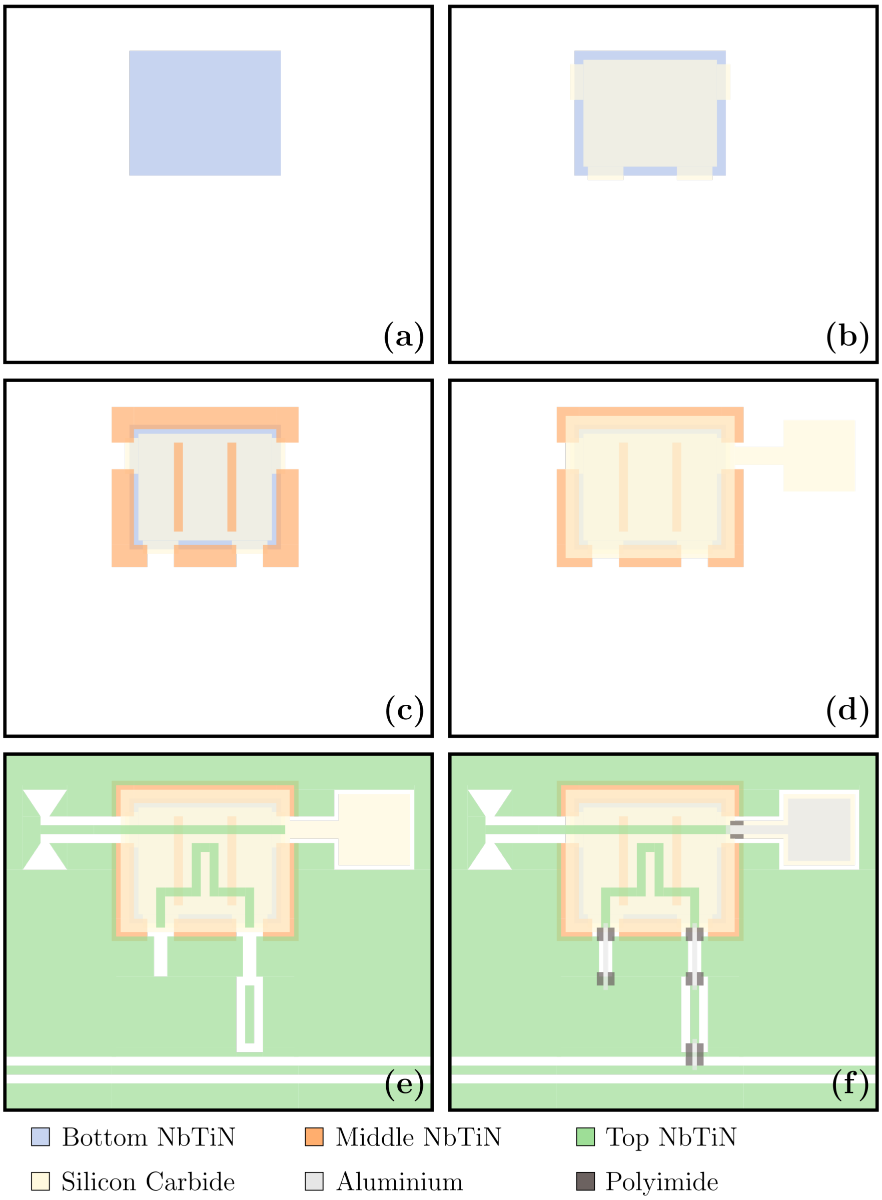

Figure 4.8: Cartoon of fabrication layer stack-up **(a)** Microstrip ground plane. **(b)** Bottom dielectric to support resonators. **(c)** Resonators and extension of ground plane. **(d)** Top dielectric to support THz line and detector line. **(e)** Antenna, MKIDs, readout CPW and THz CPW. **(f)** Aluminium for MKIDs, bridge and absorber. Intermediate polyimide step before aluminium patterning, not shown separately. Missing from this graphic: crystalline silicon substrate, silicon-nitride membrane for antenna and backside β-tantalum absorber.

connections. Furthermore, the etching rate will be slower in closely spaced mask features, so a slightly longer etch rate will ensure no residual material is left behind in such tight crevasses.

Since the test chip has a high number of layers, some layers will be exposed multiple times to the over-etch used for removing unwanted material of subsequent layers. If this happens multiple times, there is a risk of etching through a previous layer. Etching NbTiN is the most resistant layer to etch for our chip, so these layers are kept as thin as possible to make the 10% margin small. The result is that the underlying layers will experience an absolute over-etch that is smaller, compared to if a thick NbTiN layer was used. Furthermore, the layers that are deposited first are generally made thicker than the layers deposited later. For our case this has meant a relatively thick SiN layer, and a comparatively thin filterbank stack, where the top most NbTiN and SiC layers are both only 100 nm.

The fabrication process described above consists of many layers. This is largely due to extra fabrication steps to add the second SiC layer and top NbTiN to form the vertical coupling structure. A problem occurs when etching at edge transitions of previously deposited layers. The sharp angle between two layers causes an enhanced etch rate just before the transition. It is okay if the edge transition is exposed once or twice, but if it happens more, a trench will form and deepen quickly. Thin layers that are deposited later will not be able to make a sound electrical connection across this gap. The solution in our design has been to make sure each edge transition is covered by the one of the following layers, in effect covering the previous trench and moving the edge transition to the edge of the new layer.

This solution can be seen in Figure 4.8. Note how in sub-figure **(c)** the ground plane of the microstrip (sub-figure **(a)**) is extended. This covers the original edge. The new edge is from the newly deposited layer, which has not yet experienced trenching. This technique is applied at all points around the microstrip to CPW transitions.

4.3.4 Step Coverage

A second way that a poor connection can form when depositing over an edge transition is a poor step coverage. Step coverage is a term used to describe the creation of slopes at the edges of deposited layers to allow a continuous coverage of the subsequent layers. This is done by tuning etch rates, which create sloped edges. Sloped edges allow for a more gradual transition between layers and ensures a continuous growth of a subsequent layer across the edge. If the edge is too sharp and steep, the growth of a next layer will be disjointed and depositions on different layers will connect poorly.

Sloped edges are mainly created at the microstrip to CPW transitions. Here, very thin aluminium (40 nm) makes the connection across many layer edges. Due to the thinness, any sharp transition will break the line. Therefore, a good slope allows the aluminium to 'climb up' the layers. Furthermore, polyimide is deposited that forms a smooth bridge. It is deposited on these transitions, so that any sharp edge transition is avoided.

5

Preliminary Experimental Results of a Test Chip

The fabricated test chip is measured to characterize its workings. An established set-up of the THz sensing group is used that has previously been used for similar on-chip filterbank chips, which will be discussed in the Method section. The chip is measured using a scanned THz source, to sweep the full band of the filterbank on the test chip and measure the filter responses. The yield of the chip was low due to fabrication issues. In the discussion, we address these issues and propose possible solutions for them.

5.1 Method

For the measurement, the chip is cooled to 120 mK in a cryostat using dilution refrigeration from Bluefors. The cryostat has a window to allow terahertz radiation to fall on the antenna of the chip. A series of filters attenuates the signal to block out-of-band stray radiation. A specific filter cuts off the incoming signal at 400 GHz, since the radiation intensity of black-bodies at room temperatures is high above this frequency. A software package designed for use with MKIDs is used to find MKIDs and tune the readout tones.

The readout uses a local oscillator (LO) that can be tuned to a chosen frequency. Around the LO frequency, the readout tones are generated. The readout tones are fed through the chip in the cryostat. The out coming signal is down-converted using a mixer, which moves the readout tone responses to baseband. Here, an ADC records the out coming signal. The bandwidth of the system is 2 GHz. The readout tunes of the MKIDs are not always spaced within 2GHz, therefore we need separate measurements with the LO at different tunings.

Once the MKIDs are found and calibrated and an LO frequency is chosen, the measurement setup can begin. A continuous wave photomixer source is placed in front of the window, generating a tunable narrowband terahertz signal. The power of the source can be adjusted to make sure that the MKID detectors have a linear response and do not get saturated. The source is scanned across the bandwidth of the filterbank, recording the responses of each filter using the MKID detectors.

5.2 Results

The measurements were performed on chip 2 of wafer 1 of the test chip design. Only 9 MKIDs of the 50 MKIDs are found. They are identified to be the following MKIDs:

- 4 blind MKIDs
- 2 NbTiN MKIDs
- 2 Wideband MKIDs (believed to be before the filterbank)
- 1 Filter MKID

This is a very low yield. Almost all the filter MKIDs cannot be found, indicating that something went wrong where the new filter design was introduced. The reason for the low yield is a cut THz-line at the filters, which is further investigated in the discussion. The wideband MKIDs are believed to be before the filterbank, due to this reason. The blind and NbTiN MKIDs are not connected to the trough line and their function is not compromised.

The data of the filter MKID is analysed. The raw data of this MKID with the two wideband MKIDs is shown in Figure 5.1. The wideband data has three regions where it is more responsive. It is believed that these regions correspond to reflections between the antenna and the broken THz-line, which has created a standing wave between them. This energy is not easily dissipated, since the device is superconducting and no absorbing element is connected. This energy is re-radiated and finally absorbed elsewhere on the chip (e.g. in the beta-Ta absorber), which is confirmed by the blind MKIDs showing a similar response profile, albeit reduced in intensity.

Figure 5.2 shows the filter data divided by the wideband data around its resonance frequency. The low yield of the MKIDs suggests that the fault that caused the THz-line to break was a common fault on this chip. Therefore, the measured filter is believed to be the first, if not one of the first, filters in the filterbank. The measured resonance frequency is 226.9 GHz, and the loaded Q-factor is 255. If this is the first filter of the filterbank, the resonance frequency should have been 381.9 GHz. This is roughly 1.5 times the observed resonance frequency. A speculation is that, erroneously, a quarter wavelength section was connected to the resonance element due to the fabrication errors. This would cause the resonance to be two thirds of the original resonance. The remaining error can be explained by uncertainties in the material properties that were realized on the chip. Further evidence for this speculation is the secondary peak at 344.5 GHz, seen in the wideband filter response in the bottom graph of Figure 5.1. This suggests that the erroneous connection is not perfect, and a part of the signal is still resonating at the originally designed frequency due to reflections.

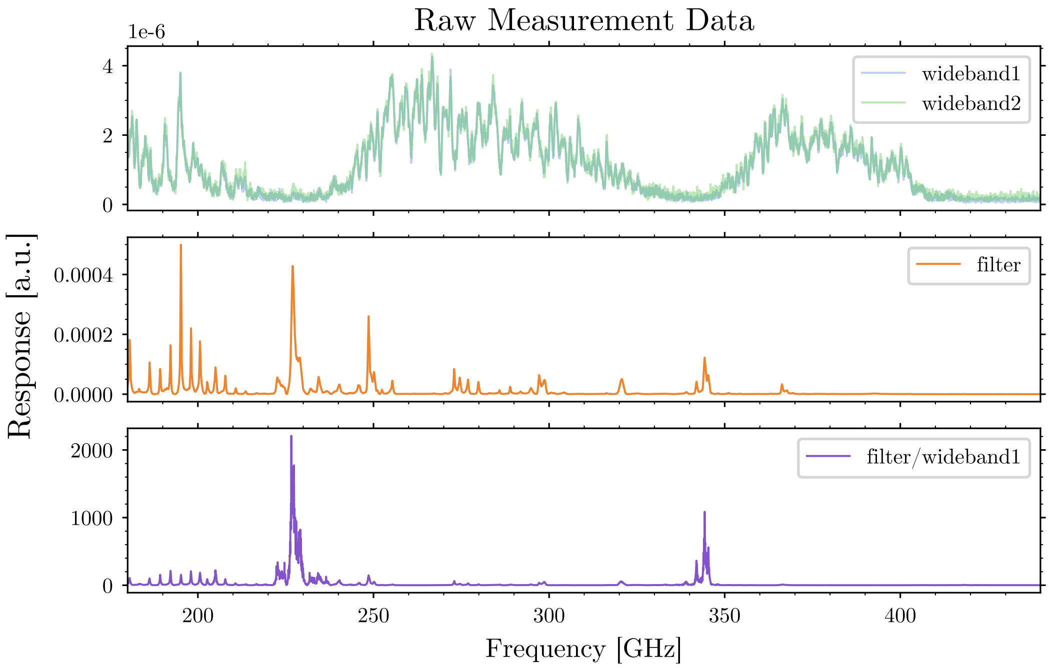

Figure 5.1: Raw data of the filter that was measured. The data was collected with a Toptica source offset at $-0.2\,\mathrm{V}$ and source amplitude at $0.7\,\mathrm{V}$. The top graph shows the response of the two wideband MKIDs. The middle graph shows the MKID filter response. The adjusted filter response is shown in the bottom graph, which is the filter response divided by the wideband response.

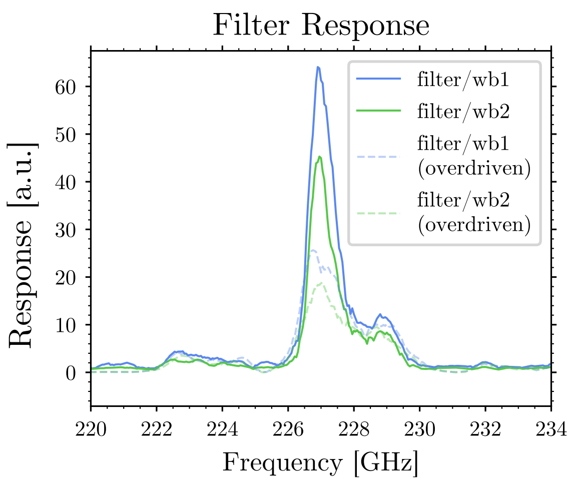

Figure 5.2: The response of the filter MKID around the filter resonance frequency. The data is normalized using the wideband MKID data and is filtered using a Savitzky-Golay smoothing filter [31] to remove noise. The response is shown for two measurements. The solid line is a low power measurement, with the Toptica source offset at $0.28\,\mathrm{V}$ and source amplitude at $0.22\,\mathrm{V}$. The dashed line is a high power measurement, with the Toptica source offset at $-0.2\,\mathrm{V}$ and source amplitude at $0.7\,\mathrm{V}$. The high power measurement causes the filter MKID to be overdriven, resulting in a non-linear response. The high power response is scaled with a factor to show the saturation the peak response overlapped with the non-saturated response. The low power measurement is used to estimate the realized resonance frequency and loaded Q-factor, which are 226.9 GHz and 255 respectively.

5.3 Discussion

To understand why there was such a low yield, scanning electron microscope (SEM) images were taken of the measured chip. Using these images, the causes contributing to the low yield of the chip are listed. A number of proposed fixes are presented to overcome these points of failure.

5.3.1 Silicon Carbide Over-Etch

In the chip design, the layers comprising the microstrip structures were deliberately chosen to be very thin. The belief being that thin layers will cause a smaller absolute over-etch and keep the step sizes between layers small. In turn, this would help with trenching and step coverage. However, the fast etch rate in silicon carbide (SiC) was not taken into account, which caused a larger than expected over-etch.

Figure 5.3 shows a SEM image after the mid-layer NbTiN deposition, patterning and etching. The layer underneath is SiC. The structure shown in the figure being one end of the resonator. Clear from this image is the over-etch into the SiC. The NbTiN layer is deposited to be around 100 nanometers thick. The over-etch is estimated to be around 100 nanometers. The SiC layer was deposited to be 200 nanometers, therefore the over-etch is significant, since it is half of the total layer thickness.

The steep edges of the SiC at the NbTiN edge indicate an anisotropic etch. A strong hint for the anisotropic etch are the "pillars" which can be seen in the figure. They are caused by the edges of the NbTiN, which sometimes have crystal structures protruding slightly. These protrusions cover a bit more of the SiC, and the SiC underneath forms a pillar after etching. It suggests that etching mainly occurs in the vertical direction only, instead of isotropical etching in all directions.

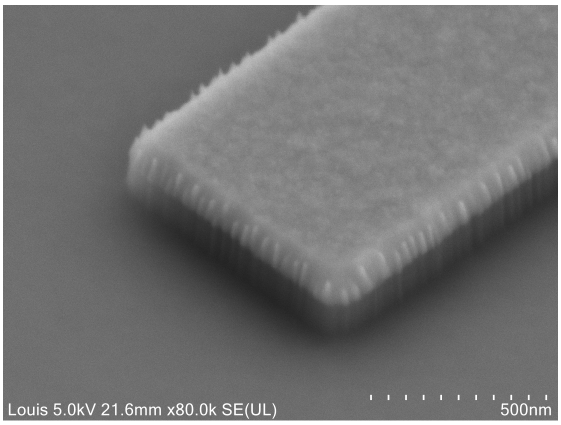

Figure 5.3: Intermediate SEM image of one end of the resonator. An over-etch can be observed in the underlying SiC.

The combination of this steep slope and the large over-etch means that it is very difficult to grow the next layer of SiC on top to have a good step coverage. The growth of the second layer of SiC starts on the flat faces of the NbTiN resonator and the first layer of SiC. A slower growth happens on the side of the steep slope. Eventually, the side growth and bottom layer growth become significant enough to leave a pocket where almost no growth happens in the corner of the structure.

In Figure 5.4 the result of this effect can be seen. This figure shows the final chip (after the top NbTiN layer is deposited and patterned as well). The NbTiN top conductor shows two distinct growth regions. At the transition a dark edge can be seen which is a steep, sharp and deep reduction in the thickness. The deposited top NbTiN layer is not able to deposit continuously across this gap. The underlying SiC growth is responsible for the steep, sharp and deep reduction in the thickness. A discontinuity is created in the conductor. The efficient transmission of the signal is blocked, and the chip is unable to function properly.

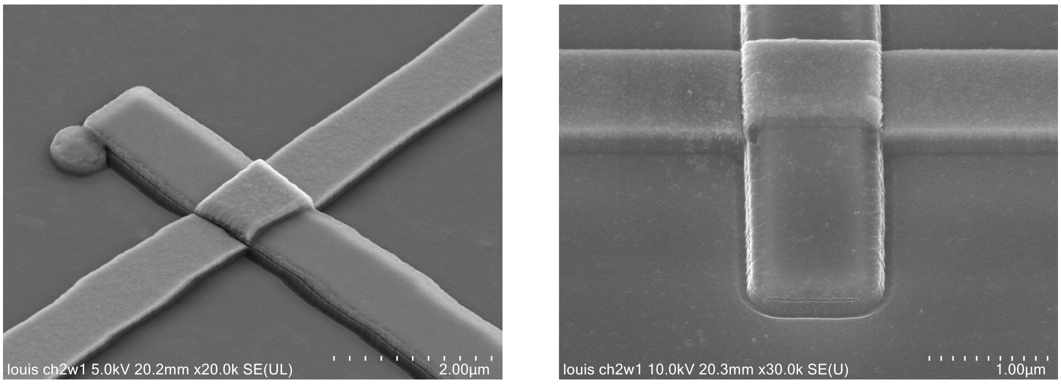

(a) Cut THz-line at 45° to the resonator

(b) Cut THz-line parallel to the resonator

Figure 5.4: One end of the resonator covered with the top layer SiC and the THz-line. The top THz-line is cut as indicated by the dark edge at the transition.

The over-etch in the SiC was not expected to be this severe, partly due to the novelty of the SiC in such a process. The fabrication of this chip has helped to better understand the characteristics of SiC. Two solutions lie at hand to solve this problem.

The first solution is using a more selective etch chemical. The current etch chemical etches the NbTiN well, but also etches the SiC (even at a faster rate). A more selective etching chemical will only etch the NbTiN or severely reduce the etching rate in SiC.

The second solution is decreasing the margin used in the etching of the NbTiN. A margin is applied to the endpoint of the etching process, to ensure all residual unwanted NbTiN is removed. However, during this period, the underlying SiC layer is also exposed to the etching chemical. Reducing the margin results in a smaller over-etch. Both solutions can be applied simultaneously to get the best result.

5.3.2 Optical and Electron-Beam Patterning Misalignment

A minor problem that was observed was the alignment of the optical and electron-beam patterning of the top-most layers. In particular, the alignment between the aluminium center line and the ground plane was off-center. Figure 5.5 shows the misalignment, which is present for all MKIDs in the fabricated test chip.

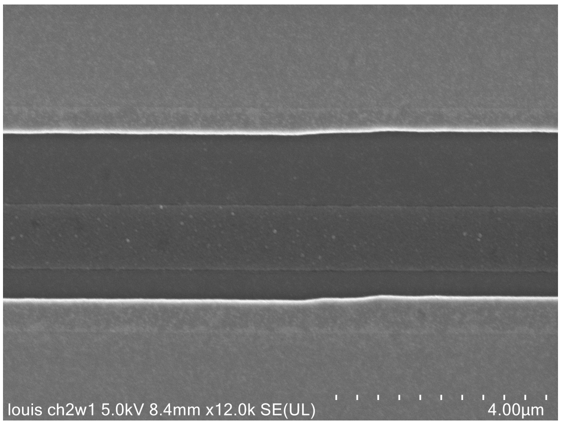

Figure 5.5: Offset of aluminium center line of the hybrid CPW section. Visible as well is a small bump in the ground plane.

The origin of this offset lies in the use of different markers for optical patterning vs electron beam patterning. The electron beam patterning uses a marker that was written by the first electron beam step, since those markers cannot be reused. However, the optical markers can be used multiple times. It is believed that the use of this secondary marker does not yield the precision required over many patterning steps to align properly. It is therefore recommended to write the edges of the ground plane of the CPW also with electron beam patterning, to ensure that the same markers are used.

6
Conclusions and Outlook

6.1 Conclusions

In this thesis, two filter concepts have been introduced as an alternative to the manifold filter, namely, the reflector filter and the directional filter. Each filter concept has been modelled as a single filter and in a filterbank configuration using microwave techniques. From the filterbank model, it is shown that the newly introduced filter types improve the coupling efficiency of a filterbank significantly. The average in-band filter efficiency of the reflector and directional filter concepts is nearly twice as efficient at around 55% when embedded in a filterbank. The reflector and directional filter reach unity transmission on resonance for an isolated filter, breaking the ideal transfer efficiency barrier of 50% that was limiting the manifold filter concept.

To find the most robust filter concept, fabrication tolerances and losses are applied to the model and each filter type is simulated in a filterbank configuration. The impact of losses is relatively equal for all filter concepts, but the directional filter concept is most robust against the modelled fabrication tolerances. The directional filter shows the least variance in its Q-factor and resonance frequency. The directional filter concept is chosen to be fabricated in a test chip.

The directional filter concept is designed using a microstrip transmission line and a vertical coupling structure to minimize coupling variances. A SONNET model is made of the design to calculate the dimensions needed for the coupling strength of the loaded Q-factor and resonance frequency. A test chip with a filterbank is fabricated with a spectral resolution of 100 across a frequency range of 200 GHz to 400 GHz.

The measurement of this chip unfortunately has shown a problem in the fabrication and only one filter was found to be responsive. The step coverage was poor across the coupling elements due to a large over-etch and steep slope. A more selective etching agent should be used with an optimization of the slope of the resonator edges to improve the step coverage.

All in all, this thesis has shown a very suitable filter solution to the problem presented in the problem statement. The directional filter shows great promise as an alternative to the manifold filter in terms of coupling efficiency. The directional filter exceeds the goal of a filter with greater than 80% efficiency by showing near unity transmission on resonance. Even with losses and fabrication tolerances, it is expected to outperform current state-of-the-art on-chip filterbanks significantly.

6.2 Outlook

The further development of the proposed filters should focus on two things, namely:

1. A successful fabrication of an on-chip filterbank chip using one of the improved filter concepts
2. Investigating higher order filters of the same concept

The successful fabrication of an on-chip filterbank with one of the improved filter concepts will give insight in the actual performance of the proposed filter concepts. One key result will be to observe the realized fabrication tolerances that are observed, and how that impacts the filterbank performance. This is still a big unknown for the current filter concepts, since the models have assumed fabrication tolerances that have been measured on a manifold filterbank. The fabrication process can be improved with each fabrication iteration, and there will be gains with doing so.

Furthermore, all filter concepts proposed in this thesis have been first order filters as observed by the roll-off of the sidebands. A higher order filter will have a sharper roll-off. This results in the filters capturing less excess noise out-of-band and overlapping less with each other, leading to an increased the efficiency.

Looking forward, the proposed designs, and future development of even higher order and therefore better filters, allow for the construction of very efficient filterbanks for an IFU. Since IFUs in the THz and far infrared band are only realistically made with on-chip technology, this is a key step forward in making large IFUs possible for present and future telescopes.

References

[1] A. Wootten, "The Atacama Large Millimeter Array (ALMA)," in *Large Ground-based Telescopes*, vol. 4837, SPIE, Feb. 4, 2003, pp. 110–118. DOI: 10.1117/12.456705.

[2] W. S. Holland, D. Bintley, E. L. Chapin, *et al.*, "SCUBA-2: The 10 000 pixel bolometer camera on the James Clerk Maxwell Telescope," *Monthly Notices of the Royal Astronomical Society*, vol. 430, no. 4, pp. 2513–2533, Apr. 21, 2013. DOI: 10.1093/mnras/sts612.

[3] J. Redford, J. Wheeler, K. Karkare, *et al.*, "The design and characterization of a 300 channel, optimized full-band millimeter filterbank for science with SuperSpec," in *Millimeter, Submillimeter, and Far-Infrared Detectors and Instrumentation for Astronomy IX*, vol. 10708, SPIE, Jul. 9, 2018, pp. 187–194. DOI: 10.1117/12.2313666.

[4] S. Bryan, J. Aguirre, G. Che, *et al.*, "WSPEC: A Waveguide Filter-Bank Focal Plane Array Spectrometer for Millimeter Wave Astronomy and Cosmology," *Journal of Low Temperature Physics*, vol. 184, no. 1, pp. 114–122, 1 Jul. 1, 2016. DOI: 10.1007/s10909-015-1396-5.

[5] G. Cataldo, E. M. Barrentine, B. T. Bulcha, *et al.*, "Second-Generation Design of Micro-Spec: A Medium-Resolution, Submillimeter-Wavelength Spectrometer-on-a-Chip," *Journal of Low Temperature Physics*, vol. 193, no. 5, pp. 923–930, 5 Dec. 1, 2018. DOI: 10.1007/s10909-018-1902-7.

[6] A. Endo, K. Karatsu, A. P. Laguna, *et al.*, "Wideband on-chip terahertz spectrometer based on a superconducting filterbank," *Journal of Astronomical Telescopes, Instruments, and Systems*, vol. 5, no. 3, p. 035 004, 3 Jun. 2019. DOI: 10.1117/1.JATIS.5.3.035004.

[7] C. N. Thomas, S. Withington, R. Maiolino, *et al.*, *The CAMbridge Emission Line Surveyor (CAMELS)*, Jan. 17, 2014. DOI: 10.48550/arXiv.1401.4395.

[8] A. Endo, K. Karatsu, Y. Tamura, *et al.*, "First light demonstration of the integrated superconducting spectrometer," *Nature Astronomy*, vol. 3, no. 11, pp. 989–996, 11 Nov. 2019. DOI: 10.1038/s41550-019-0850-8.

[9] A. Einstein, "The Theory of Special Relativity," 1922. DOI: 10.1007/978-94-011-6022-3_2.

[10] J. A. Hodge and E. da Cunha, "High-redshift star formation in the Atacama large millimetre/submillimetre array era," *Royal Society Open Science*, vol. 7, no. 12, p. 200 556, 12 Aug. 22, 2022. DOI: 10.1098/rsos.200556.

[11] M. R. Blanton, "Sloan Digital Sky Survey IV: Mapping the Milky Way, Nearby Galaxies, and the Distant Universe," *The Astronomical Journal*, p. 35, 2017.

[12] P. J. De Visser, "Quasiparticle dynamics in aluminium superconducting microwave resonators," 2014.

[13] R. M. J. Janssen, J. J. A. Baselmans, A. Endo, *et al.*, "High optical efficiency and photon noise limited sensitivity of microwave kinetic inductance detectors using phase readout," *Applied Physics Letters*, vol. 103, no. 20, p. 203 503, 20 Nov. 11, 2013. DOI: 10.1063/1.4829657.

[14] J. Bardeen, L. N. Cooper, and J. R. Schrieffer, "Theory of Superconductivity," *Physical Review*, vol. 108, no. 5, pp. 1175–1204, 5 Dec. 1, 1957. DOI: 10.1103/PhysRev.108.1175.

[15] P. K. Day, H. G. LeDuc, B. A. Mazin, A. Vayonakis, and J. Zmuidzinas, "A broadband superconducting detector suitable for use in large arrays," *Nature*, vol. 425, no. 6960, pp. 817–821, 6960 Oct. 2003. DOI: 10.1038/nature02037.

[16] A. Pascual Laguna, K. Karatsu, D. J. Thoen, *et al.*, "Terahertz Band-Pass Filters for Wideband Superconducting On-Chip Filter-Bank Spectrometers," *IEEE Transactions on Terahertz Science and Technology*, vol. 11, no. 6, pp. 635–646, 6 Nov. 2021. DOI: 10.1109/TTHZ.2021.3095429.

[17] A. Pascual Laguna, "On-Chip Solutions for Future THz Imaging Spectrometers," 2022. DOI: 10.4233/uuid:512da833-dc9d-4301-b566-35243d2f1f9b.

[18] D. M. Pozar, *Microwave Engineering*, 4th ed. Hoboken, NJ: Wiley, 2012, 732 pp.

[19] G. L. Matthaei, L. Young, and E. M. T. Jones, *Microwave Filters, Impedance-Matching Networks, and Coupling Structures*, Reprint of the ed. publ. by MacGraw-Hill 1964, ser. The Artech House Microwave Library. Norwood, Mass: Artech House, 1985, 1096 pp.

[20] S. B. Cohn and F. S. Coale, "Directional Channel-Separation Filters," *Proceedings of the IRE*, vol. 44, no. 8, pp. 1018–1024, Aug. 1956. DOI: 10.1109/JRPROC.1956.275043.

[21] L. Tuttle and R. Wanselow, "Practical Design of Strip-Transmission-Line Half-Wavelength Resonator Directional Filters," *IRE Transactions on Microwave Theory and Techniques*, vol. 7, no. 1, pp. 168–173, Jan. 1959. DOI: 10.1109/TMTT.1959.1124642.

[22] O. Wing, "Cascade Directional Filter," *IRE Transactions on Microwave Theory and Techniques*, vol. 7, no. 2, pp. 197–201, Apr. 1959. DOI: 10.1109/TMTT.1959.1124681.

[23] J. P. Kim, "Improved Design of Single-Section and Cascaded Planar Directional Filters," *IEEE Transactions on Microwave Theory and Techniques*, vol. 59, no. 9, pp. 2206–2213, Sep. 2011. DOI: 10.1109/TMTT.2011.2160871.

[24] M. Frankel, S. Gupta, J. Valdmanis, and G. Mourou, "Terahertz attenuation and dispersion characteristics of coplanar transmission lines," *IEEE Transactions on Microwave Theory and Techniques*, vol. 39, no. 6, pp. 910–916, 6 Jun. 1991. DOI: 10.1109/22.81658.

[25] S. Hähnle, N. v. Marrewijk, A. Endo, *et al.*, "Suppression of radiation loss in high kinetic inductance superconducting co-planar waveguides," *Applied Physics Letters*, vol. 116, no. 18, p. 182 601, 18 May 4, 2020. DOI: 10.1063/5.0005047.

[26] B. T. Buijtendorp, S. Vollebregt, K. Karatsu, *et al.*, *Hydrogenated Amorphous Silicon Carbide: A Low-loss Deposited Dielectric for Microwave to Submillimeter Wave Superconducting Circuits*, Oct. 7, 2021. DOI: 10.48550/arXiv.2110.03500.

[27] A. Endo, A. P. Laguna, S. Hähnle, *et al.*, "Simulating the radiation loss of superconducting submillimeter wave filters and transmission lines using Sonnet EM," in *Millimeter, Submillimeter, and Far-Infrared Detectors and Instrumentation for Astronomy X*, Dec. 13, 2020, p. 82. DOI: 10.1117/12.2560458.

[28] A. Taniguchi, T. J. L. C. Bakx, J. J. A. Baselmans, *et al.*, *DESHIMA 2.0: Development of an integrated superconducting spectrometer for science-grade astronomical observations*, Oct. 27, 2021. DOI: 10.48550/arXiv.2110.14656.

[29] S. Shu, M. Calvo, J. Goupy, *et al.*, "Increased multiplexing of superconducting microresonator arrays by post-characterization adaptation of the on-chip capacitors," *Applied Physics Letters*, vol. 113, no. 8, p. 082 603, Aug. 20, 2018. DOI: 10.1063/1.5040968.

[30] S. O. Dabironezare, K. Karatsu, S. Yates, *et al.*, "Wide Band Quasi-Optical System for DESHIMA 2.0 Spectrometer: Beam Pattern Experimental Validation," in *2020 45th International Conference on Infrared, Millimeter, and Terahertz Waves (IRMMW-THz)*, Nov. 2020, pp. 1–1. DOI: 10.1109/IRMMW-THz46771.2020.9371005.

[31] A. Savitzky and M. J. E. Golay, "Smoothing and Differentiation of Data by Simplified Least Squares Procedures.," *Analytical Chemistry*, vol. 36, no. 8, pp. 1627–1639, 8 Jul. 1, 1964. DOI: 10.1021/ac60214a047.

[32] M. J. Griffin, A. Abergel, A. Abreu, *et al.*, "The Herschel-SPIRE instrument and its in-flight performance," *Astronomy & Astrophysics*, vol. 518, p. L3, Jul. 1, 2010. DOI: 10.1051/0004-6361/201014519.

A
Size Comparison of Spectrometers

Two implementations of an imaging spectrometer in the THz band can realistically be considered. The first is a Fourier-transform spectrometer (FTS), like the Hershel SPIRE instrument [32]. The second is the on-chip filter-bank, like the DESHIMA instrument [6]. This section will illustrate the significant advantage that an on-chip spectrometer has, in comparison with an FTS.

Briefly, the principle of an on-chip spectrometer is as follows. The signal is coupled to a chip using an antenna. Here, the signal is confined to a waveguide, such as a microstrip or a co-planar waveguide. Then, the signal is filtered on-chip using a filter bank. The filter bank outputs are coupled to detectors. Due to the signal being confined to the chip, all signal manipulations are greatly miniaturized. This, in turn, means that many such structures can be made on a single chip with many lenses, each lens coupling to an on-chip spectrometer. In such a way, a 2D image can be captured instantly with spectral information for each pixel.

The FTS takes a different approach. The incoming signal is split and sent to two mirrors. One mirror is moved across a range of positions, the other is kept at a constant distance, changing the relative path difference. This creates an interference. Measuring this interference across a range of positions gives an interference pattern. This interference pattern is Fourier-transformed and the result is the spectrum of the source. This whole sequence can be performed simultaneously for a 2D image.

The comparative advantage between these two designs is the physical footprint. To resolve two frequencies, the path difference must be long enough. This is called the disambiguation distance Δd and it is given by

$$\Delta d = \frac{1}{2} \times \lambda \frac{\lambda}{\Delta\lambda}, \tag{A.1}$$

where λ is the wavelength of the center frequency and $\Delta\lambda$ is the difference of wavelength between the two frequencies. For sub-mm/THz wavelengths, this disambiguation distance is around 0.5 m for R equalling 1000. This is roughly the size of an FTS at THz frequencies. For an on-chip filterbank the disambiguation distance is folded Q times in the bandpass filter. Where Q is the quality factor of the filter. Furthermore, the wavelength inside the chip scales with $1/\sqrt{\varepsilon_r}$, meaning that the wavelength is roughly 3 times shorter for silicon based devices.

The footprint of an on-chip spectrometer is several orders of magnitude smaller than an FTS. A comparison is given in Figure A.1 between the Herschel-SPIRE instrument and the DESHIMA on-chip single pixel spectrometer. The DESHIMA has an approximate size of 50 mm, whereas the Herschel-SPIRE instrument has a length of about 700 mm, with similar spectral resolutions.

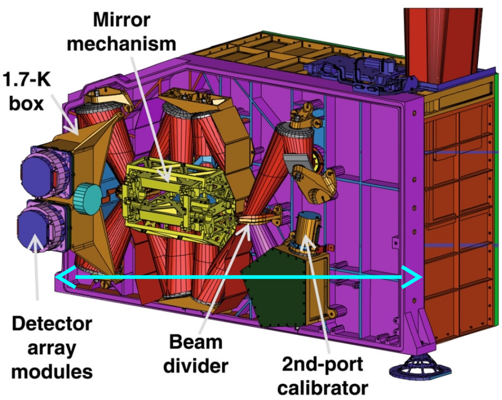

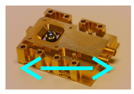

On-chip spectrometer $\sim$ 50 mm

Fourier tranform spectrometer $\sim$ 700 mm

Figure A.1: FTS vs on-chip spectrometer size comparison (not to scale).

Next generation on-chip spectrometer designs aim to fit hundreds of spectrometers on 50 mm wafers, filling the field-of-view of the telescope. An FTS spectrometer that fills the field-of-view with detectors is required to scan in frequency. The on-chip spectrometer has no such limitations and can freely choose the number of detectors in the frequency dimension. Resulting in a greater total number of detectors that can measure simultaneously. The biggest drawback is that the individual detectors have to be R times as sensitive as the FTS detectors, but MKIDs have shown very good sensitivities already. Therefore, the on-chip spectrometer is the best suited spectrometer configuration that can truly be used in a future IFU concept.

B

Calculations to find the Coupling Capacitor Strength and Resonator Length

Figure B.1 shows a resonator which we would like to hav a certain resonance frequency and loaded Q-factor. The resonance frequency is given by f_0 and the loaded Q-factor is given by Q_L. First the calculations for the coupling strength are given, then the formulas for the resonator length are given.

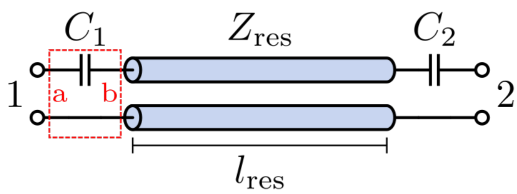

Figure B.1: A resonator.

B.1 Coupling Strength

The loaded Q-factor is defined in Section 2, Equation 2.1, and is repeated here:

$$Q_{\mathrm{L}} = 2\pi f_0 \frac{E_{\mathrm{stored}}}{P_{\mathrm{lost}}}. \tag{B.1}$$

Given $l_{\mathrm{res}} \approx n\lambda/2$, where n is a positive integer, the power leaking per cycle of a doubly coupled resonator is

$$P_{\mathrm{lost}} = \frac{2}{n} f_0 E_{\mathrm{stored}} |S_{\mathrm{ab}}|^2. \tag{B.2}$$

$|S_{\mathrm{ab}}|^2$ is the transmission from b to a, as defined by the red box in Figure B.1. The loading of the red box is $Z_{\mathrm{a}} = Z_1$ and $Z_{\mathrm{b}} = Z_{\mathrm{res}}$. The factor two follows from the fact that a coupling element is encountered $2/n$ times per cycle (a wave travelling one wavelength).

Now, adding Equation B.2 to Equation B.1 gives us the following relation between Q_L and $|S_\mathrm{ab}|^2$

$$Q_\mathrm{L} = \frac{n\pi}{|S_\mathrm{ab}|^2}. \tag{B.3}$$

Finally, the losses in the system are also added, and the inverse of the above formula can be given in terms of Q_c or Q_L. In a two-sided equal coupling half-wave resonator, this inverse relation is as follows. Starting from

$$Q_\mathrm{L}^{-1} = Q_\mathrm{i}^{-1} + 2Q_\mathrm{c}^{-1},$$

if $Q_\mathrm{c} \ll Q_\mathrm{i}$, then

$$Q_\mathrm{L} = \frac{Q_\mathrm{c}}{2},$$

which leads to:

$$|S_\mathrm{ab}|^2 = \frac{2\pi}{Q_\mathrm{c}}. \tag{B.4}$$

For different configurations, the energy loss mechanism might differ. For one, the factor two in Equation B.2 should be removed if the device has an uncoupled open end at the resonator. A second case is a shorted resonator, in this case the resonance condition length is defined as $l_\mathrm{res} \approx n\lambda/4$, and it is only coupled on one side of the resonator. When adjusting the power loss mechanisms, a singly coupled quarter-wave resonator has the same power lost per cycle as a doubly coupled half-wave resonator, since in both cases a coupling element is encountered twice per cycle. This is useful since the same formula can be used for designing the coupler for the reflector in the reflector filter concept.

B.1.1 Ideal Capacitor

The loaded Q-factor is tuned to match the design value by finding the capacitance value that corresponds to the right $|S_\mathrm{ab}|^2$ transmission. In the circuit model, the coupling capacitor is considered an ideal capacitor. The loading of this capacitor is given by the impedances $Z_\mathrm{a} = Z_1$ and $Z_\mathrm{b} = Z_\mathrm{res}$. The impedance of an ideal capacitor is $Z = (j2\pi f_0 C)^{-1}$, and is used to derive the relation between S_ab and C as being

$$S_\mathrm{ab} = \frac{2\sqrt{R_\mathrm{a}R_\mathrm{b}}}{Z_\mathrm{a} + (j2\pi f_0 C)^{-1} + Z_\mathrm{b}}, \tag{B.5}$$

where R_a and R_b are the real parts of their respective loading impedances. Squaring and inverting this formula gives the coupling capacitance for a given $|S_\mathrm{ab}|^2$ and therefore for a given Q_L.

B.1.2 Simulated Coupling Structure

For a simulated coupler using SONNET, the S-parameters can be extracted. However, due to the nature of the coupling structure, the relations change slightly. In Figure B.2 the structure and ports, indicated by i, j and k, can be seen. The green line indicates the top through line. The orange line is one of the ends of the resonator. A vertical coupling structure is implemented. With the resonator embedded between two dielectric layers. The ground plane is at the bottom and the trough line on top.

Looking at the equivalent circuit, the energy exchange of the resonator with the through line is captured in two S-parameters, namely $|S_{\mathrm{ij}}|^2$ and $|S_{\mathrm{kj}}|^2$. Which leads to $|S_{\mathrm{ab}}|^2 = |S_{\mathrm{ij}}|^2 + |S_{\mathrm{kj}}|^2$ for the simulated structure to match with the coupling formulas described above. Furthermore, due to symmetry, $|S_{\mathrm{ij}}|^2 = |S_{\mathrm{kj}}|^2$. All in all, the coupling relation to Q_{c} is now described as

$$|S_{\mathrm{ij}}|^2 = \frac{|S_{\mathrm{ab}}|^2}{2} = \frac{2\pi}{2Q_{\mathrm{c}}}. \tag{B.6}$$

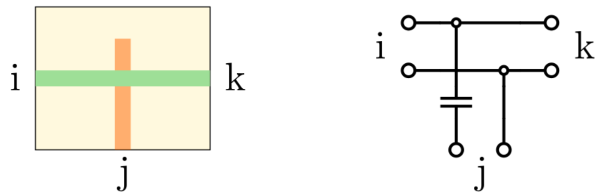

Figure B.2: Simulated SONNET structure and equivalent circuit for a coupler used in the resonating elements.

B.2 Resonator Length

Finally, the resonator length is found by finding $\mathrm{Im}\{Z_{\mathrm{in}}\} = 0$ at the resonance frequency. Z_{in} is taken at port 1 of Figure B.1 and ports 1 and 2 are loaded with the appropriate impedance, depending on the filter type. The previously calculated capacitances are added as well and their impedance is given by $Z = (j2\pi f_0 C)^{-1}$.

C
Filterbank Model Results

Filterbank model results for each filter type.

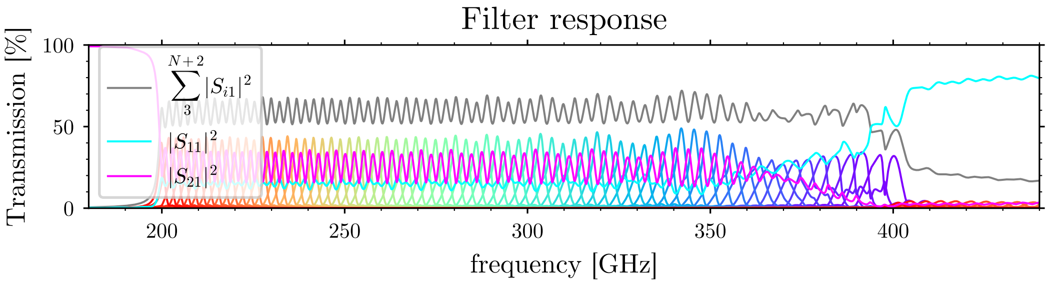

Figure C.1: Manifold Filter - Filterbank

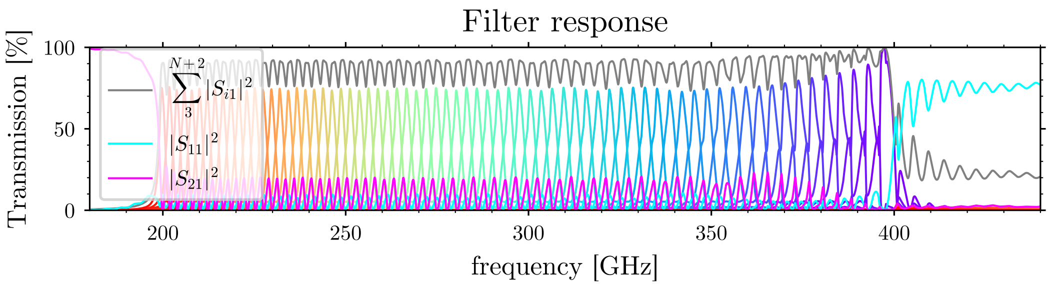

Figure C.2: Reflector Filter - Filterbank

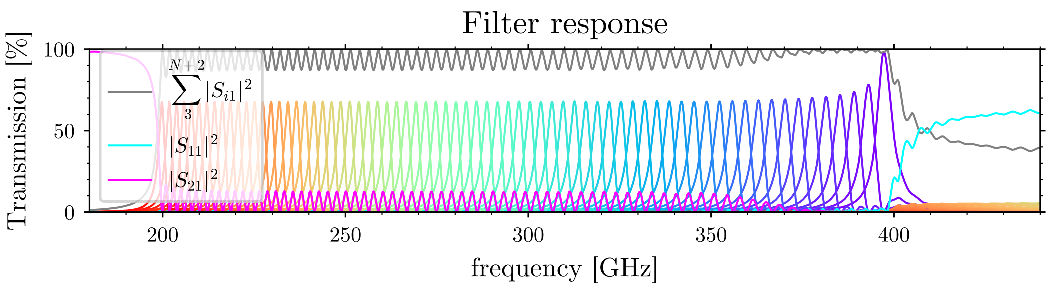

Figure C.3: Directional Filter - Filterbank

D

Filterbank Model Results with Variances

Filterbank model results with variances for each filter type. An f_i variance of 20% around its nominal value and a Q_L variance of 10% around its nominal value is applied.

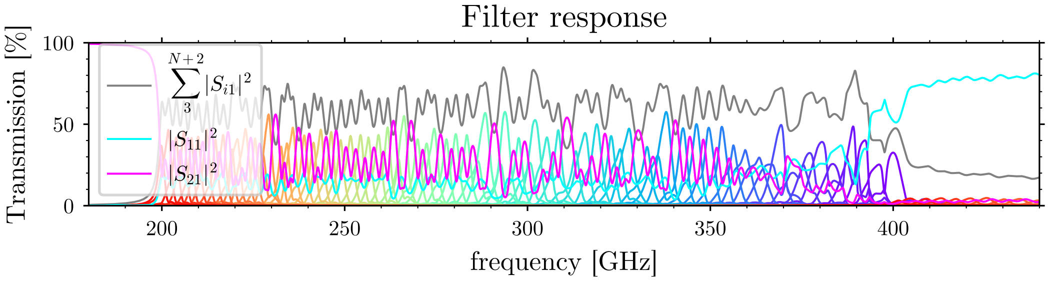

Figure D.1: Manifold Filter - Filterbank

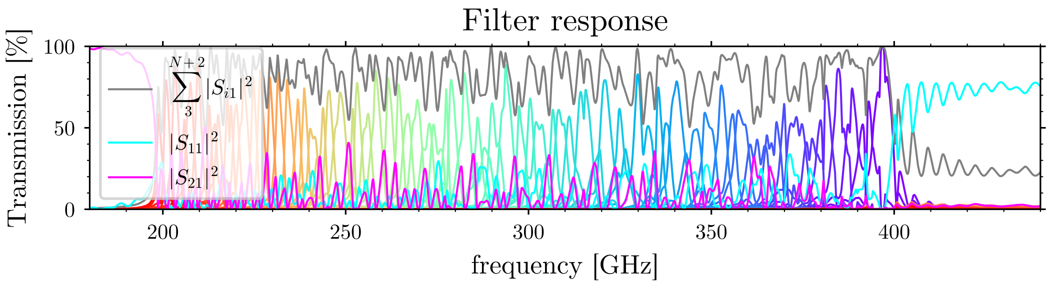

Figure D.2: Reflector Filter - Filterbank

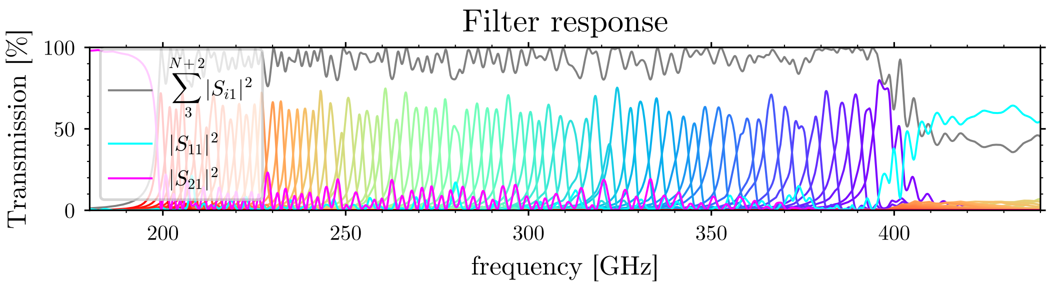

Figure D.3: Directional Filter - Filterbank